Received: 26 November 2021 | Revised: 22 April 2022 | Accepted: 5 May 2022

DOI: 10.1002/nag.3408

RESEARCH ARTICLE

WILEY

Multi-phase-field microporomechanics model for simulating ice-lens growth in frozen soil

Hyoung Suk Suh | **WaiChing Sun**

Department of Civil Engineering and Engineering Mechanics, Columbia University, New York, NY, USA

Correspondence
WaiChing Sun, Department of Civil Engineering and Engineering Mechanics, Columbia University, 614 SW Mudd, 4709, New York, NY 10027, USA.
Email: wsun@columbia.edu

Funding information
Army Research Office, Grant/Award Number: W911NF-18-2-0306; Division of Civil, Mechanical and Manufacturing Innovation, National Science Foundation, Grant/Award Number: 1846875

Abstract

This article presents a multi-phase-field poromechanics model that simulates the growth and thaw of ice lenses and the resultant frozen heave and thaw settlement in multi-constituent frozen soils. The growth of segregated ice inside the freezing-induced fracture is implicitly represented by the evolution of two-phase fields that indicate the locations of segregated ice and the damaged zone, respectively. The evolution of two-phase fields is induced by their own driving forces that capture the physical mechanisms of ice and crack growths, respectively, while the phase-field governing equations are coupled with the balance laws such that the coupling among heat transfer, solid deformation, fluid diffusion, crack growth, and phase transition can be replicated numerically. Unlike phenomenological approaches that indirectly capture the freezing influence on the shear strength, the multiphase-field model introduces an immersed approach where both the homogeneous freezing and the ice-lens growth are distinctively captured by the freezing characteristic function and the driving force accordingly. Verification and validation examples are provided to demonstrate the capacities of the proposed models.

KEYWORDS
frozen soil, ice lens, phase field, phase transition, thermo-hydro-mechanics

1 | INTRODUCTION

Ice-lens formation at the microscopic scale is a physical phenomenon critical for understanding the physics of frost heave and thawing settlement occurred at the field scale under the thermal cycles. Since ice lens may affect the freeze–thaw action and cause frost heave and thawing settlement sensitive to the changing climate and environment conditions, knowledge on the mechanism for the ice-lens growth is of practical value for many civil engineering applications in cold regions.[1–5] For example, substantial heaving and settlement caused by the sequential formations and thawing of ice lenses lead to uneven deformation of the road, which also damages the tires, suspension, and ball joints of vehicles. In the United States alone, it was estimated that two billion dollars had been spent annually to repair frost damage of roads.[6] Moreover, extreme climate change over the last few decades has brought increasing attention to permafrost degradation, since unusual heat waves may cause weakening of foundations and increase the likelihood of landslides triggered by the abrupt melting of the ice lens.[7–11] Under these circumstances, both the fundamental understanding of the ice-lens growth mechanisms and the capacity to predict and simulate the effect beyond the one-dimensional models becomes increasingly important.

Since the pioneering work on the ice lens by Stephan Taber in the early 20th century,[12,13] there has been a considerable amount of progress in the geophysics and fluid mechanics community to elucidate the mechanisms in the ice segregation process (e.g.,Peppin and Style[14] and references cited therein). During the freezing phase, it is now known that the crystallized pore ice surrounded by a thin premelted water film develops a suction pressure (i.e., cryo-suction) that attracts the unfrozen water towards the freezing front[15–17]. These films remain unfrozen below the freezing temperature and form an interconnected flow network that supplies water to promote ice crystal growth. Accumulation of pore ice crystals accompanies the void expansion and micro-cracking of the host matrix, which may result in the formation of a horizontal lens of segregated ice. However, despite these substantial amounts of work, the criterion for the ice-lens initiation and its detailed mechanism still remains unclear. Based on the thermo-hydraulic model proposed by Harlan,[18] Miller[19–21] introduces a concept of stress partitioning and assumed that an ice lens starts to form if the solid skeleton experiences tensile stress. This idea has been further adopted and further generalized in Refs.[22,23] via an asymptotic method. Gilpin[24] suggests that the ice-lens formation takes place when the ice pressure reaches the particle separation pressure depending on the particle size and the interfacial tension between the water and ice, whereas Zhou and Li[25] propose the idea of separation void ratio as a criterion for the ice lensing. Konrad and Morgenstern[26] present an alternative approach that can describe the formation and growth of a single ice lens based on segregation potential, of which the applicability has been demonstrated in Refs.[27–29] On the other hand, Rempel[30,31] develops regime diagrams that delineate the growth of a single lens, multiple lenses, and homogeneous freezing. In this line of work, the one-dimensional momentum and mass equilibrium equations are coupled with the heat flow in a step-freezing Stefan configuration to calculate the intermolecular force that drives the premelted fluid to the growing ice lenses. While the proposed method is helpful for estimating the lens thickness and spacing, the one-dimensional setting is understandably insufficient for the geo-engineering applications that require understanding of the implication of ice lenses on the shear strength. More recently, Style et al.[32] propose a new theory on the ice-lens nucleation by considering the cohesion of soil and the geometric supercooling of the unfrozen water in the pore space. Although the aforementioned studies formed the basis to shed light on explaining the ice-lens formation, they are limited to the idealized one-dimensional problems and often idealized soil as a linear elastic material and hence not sufficient for applications that require a more precise understanding of the constitutive responses of the ice-rich soil.

Meanwhile, within the geomechanics and geotechnical engineering community, a number of theories and numerical modeling frameworks have been proposed based on the mixture theory and thermodynamics principles[33–36] with a variety of complexities and details. By adopting the premelting theory and considering the frozen soil as a continuum mixture of the solid, unfrozen water, and ice constituents, the freezing retention behavior of frozen soil can be modeled in a manner similar to those for the unsaturated soil. The resultant finite element implementation of these models enables us to simulate freeze-thaw effects in two- or three-dimensional spaces often with more realistic predictions on the solid constitutive responses. Nevertheless, the presence of crystal ices in the pores and that inside the expanded ice lens is often represented via phenomenological laws.[36,37] Since the morphology, physics, and the mechanisms as well as the resultant mechanical characteristics of the ice lens and ice crystals in pores are profoundly different, it remains difficult to develop a predictive phenomenological constitutive law for an effective medium that represents the multi-constituent frozen soil with ice lenses.[38]

This study is an attempt to reconcile the fluid mechanics and geotechnical engineering modeling efforts on modeling the frozen soil under changing climates. Our goal is to (1) extend the field theory for ice lens such that it is not restricted to one-dimensional problems and (2) introduce a framework that may incorporate more realistic path-dependent constitutive laws. As such, the coupling mechanism among phase transition, fluid diffusion, heat transfer, and solid mechanics can be captured without solely relying on phenomenological material laws. In particular, we introduce a mathematical framework and a corresponding finite element solver that may distinctively capture the physics of ice lens and freezing/thawing. We leverage the implicit representation of complex geometry afforded by a multiphase-field framework to first overcome the difficulty of capturing the evolving geometry of the ice lens. By considering the ice lens as segregated bulk ice inside the freezing-induced fracture, we adopt two-phase field variables that represent the state of the fluid phase constituent and the regularized crack topology, respectively. This treatment enables us to take account of the brittle fracture that may occur during ice-lens growth and explicitly incorporate the addition and vanishing shear strength and bearing capacity of the ice lens under different environmental conditions. The phase transition of the fluid is modeled via the Allen–Cahn equation,[39,40] while we adopt the phase-field fracture framework to model brittle cracking in a solid matrix.[41–43] The resultant framework may provide a fuller picture to analyzing the growth of the ice lens in the frozen soil, while verification exercises also confirm that the model may reduce to a classical thermo-hydro-mechanical model and isothermal poromechanics model under limited conditions.

The rest of the paper is organized as follows. Section 2 summarizes the necessary ingredients for the mathematical framework, while we present the multi-phase-field microporomechanics model that describes the coupled behavior of a fluid-saturated phase-changing porous media in Section 3. For completeness, the details of the finite element formulation and the operator splitting solution strategy are discussed in Section 4. Finally, numerical examples are given in Section 5 to verify, validate, and showcase the model capacity, which highlights its potential by simulating the growth and melting of multiple ice lenses.

As for notations and symbols, bold-faced and blackboard bold-faced letters denote tensors (including vectors which are rank-one tensors); the symbol "$\cdot$" denotes a single contraction of adjacent indices of two tensors (e.g., $\boldsymbol{a}\cdot\boldsymbol{b}=a_ib_i$ or $\boldsymbol{c}\cdot\boldsymbol{d}=c_{ij}d_{jk}$); the symbol ":" denotes a double contraction of adjacent indices of tensor of rank two or higher (e.g., $\mathbb{C}:\boldsymbol{\varepsilon}=C_{ijkl}\varepsilon_{kl}$); the symbol "$\otimes$" denotes a juxtaposition of two vectors (e.g., $\boldsymbol{a}\otimes\boldsymbol{b}=a_ib_j$) or two symmetric second-order tensors [e.g., $(\boldsymbol{\alpha}\otimes\boldsymbol{\beta})_{ijkl}=\alpha_{ij}\beta_{kl}$]. We also define identity tensors: $\boldsymbol{I}=\delta_{ij}$, $\mathbb{I}=\delta_{ik}\delta_{jl}$, and $\bar{\mathbb{I}}=\delta_{il}\delta_{jk}$, where δ_{ij} is the Kronecker delta. As for sign conventions, unless specified, tensile stress and dilative pressure are considered positive.

2 | KINEMATICS AND EFFECTIVE STRESS PRINCIPLE FOR FROZEN SOIL WITH ICE LENS

In this section, we introduce the ingredients necessary to derive the field theory for the phase-field modeling of frozen soil presented later in Section 3. Similar to the treatments in Refs.[33–35], we first assume that the frozen soil is fully saturated with either water or ice and therefore idealize the frozen soil as a three-phase continuum mixture that consists of solid, water, and ice-phase constituents whereas the ice lens is a special case in which the solid skeleton no longer holds bearing capacity. This treatment enables us to formulate a multiphase-field approach to employ two-phase field variables as indicator functions for the state of the pore fluid (in ice or water form)[40,44,45] and that of the solid skeleton (in damage or intact form).[41–43] We then extend the effective stress theory originated from damage mechanics[46] to incorporate the internal stress of ice lenses caused by the deformation of the effective medium into the Bishop's effective stress principle for frozen soil where the introduction of phase-field provides smooth transition of the material states for both the pore fluid and the solid skeleton. This procedure allows us to incorporate both the capillary pressure of the ice crystal surrounded by the water thin film as well as the volumetric and deviatoric stresses triggered by the deformation of the ice lens.

2.1 | Continuum representation and kinematics

Based on the mixture theory, we idealize our target material as a multiphase continuum where the solid-, water-, and ice-phase constituents are overlapped. For simplicity, this study assumes that there is no gas phase inside the pore such that the pore space is either occupied by water or ice. The volume fractions of each phase constituent are defined as

$$\phi^s=\frac{dV_s}{dV};\phi^w=\frac{dV_w}{dV};\phi^i=\frac{dV_i}{dV};\phi^s+\sum_{\alpha=\{w,i\}}\phi^\alpha=1, \tag{1}$$

where the indices s, w, and i refer to the solid-, water-, and ice-phase constituents, respectively, while $dV=dV_s+dV_w+dV_i$ denote the total elementary volume of the mixture. Note that an index used as a subscript indicates the intrinsic property of a phase constituent, while it is used as a superscript when referring to a partial property of the entire mixture. By letting ρ_s, ρ_w, and ρ_i denote the intrinsic mass densities of the solid, water, and ice, respectively, the partial mass densities of each phase constituent are given by

$$\rho^s=\phi^s\rho_s;\rho^w=\phi^w\rho_w;\rho^i=\phi^i\rho_i;\rho^s+\sum_{\alpha=\{w,i\}}\rho^\alpha=\rho, \tag{2}$$

where ρ is the total mass density of the entire mixture. We also define the saturation ratios for the fluid phase constituents $\alpha=\{w,i\}$ as

$$S^w=\frac{\phi^w}{\phi};S^i=\frac{\phi^i}{\phi};\sum_{\alpha=\{w,i\}}S^\alpha=1, \tag{3}$$

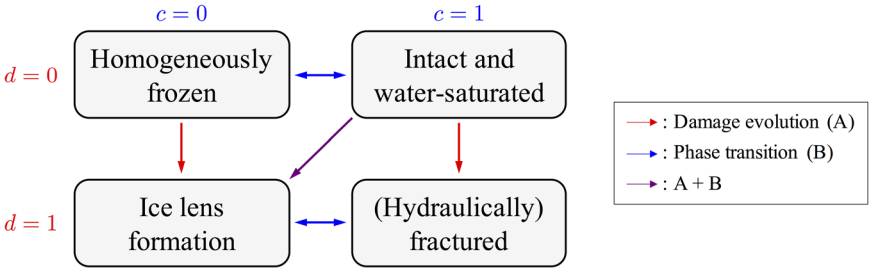

FIGURE 1 Schematic of multiphase-field approach coupled with a thermo-hydro-mechanical model

where $\phi = 1 - \phi^s$ is the porosity.

Since the solid (s), water (w), and ice (i) phases do not necessarily follow the same trajectory, each constituent possesses its own Lagrangian motion function that maps the position vector of the current configuration $\boldsymbol{x}$ at time t to their reference configurations. In this study, we adopt a kinematic description that traces the motion of the solid matrix by following the classical theory of porous media.[47–50] Hence, the motion of the solid phase is described by using the Lagrangian approach via its displacement vector $\boldsymbol{u}(\boldsymbol{x}, t)$, whereas the fluid phase ($\alpha = \{w, i\}$) motions are described by the modified Eulerian approach via relative velocities $\tilde{\boldsymbol{v}}_w$ and $\tilde{\boldsymbol{v}}_i$, instead of their own velocity fields $\boldsymbol{v}_w$ and $\boldsymbol{v}_i$, that is,

$$\tilde{\boldsymbol{v}}_\alpha = \boldsymbol{v}_\alpha - \boldsymbol{v}, \tag{4}$$

where $\boldsymbol{v} = \dot{\boldsymbol{u}}$ is the solid velocity, while $\dot{(\bullet)} = \mathrm{d}(\bullet)/\mathrm{d}t$ is the total time derivative following the solid matrix.

2.2 | Multiphase-field approximation of freezing-induced crack

In this current study, we assume that the path-dependent constitutive responses of the frozen soil is due to the fracture in the brittle regime and the growth/thaw of the ice lens in the void space that could be opened by the expanded ice. While plasticity of the solid skeleton as well as the damage and creeping of the segregated ice may also play important roles on the mechanisms of the frost heave and thaw settlement, they are out of the scope of this study. As such, this study follows Miller's theory, which assumes that a new ice lens may only form if and only if the compressive effective stress becomes zero or negative.[19–21,51] Since opening up the void space is a necessary condition for the ice lens to grow inside, we introduce a phase-field model that captures the crack growth potentially caused by the ice lenses growth. In this work, our strategy is to adopt diffuse approximations for both the phase transition of the pore fluid and the crack topology, where each requires a distinct phase-field variable. As illustrated in Figure 1, introducing two-phase fields not only enables us to distinguish the homogeneous freezing from the ice-lens growth but also leads to a framework that can be considered as a generalization of a thermo-hydro-mechanical model.

The first phase-field variable $c \in [0, 1]$ used in this study is an order parameter that models the freezing of water (melting of ice) in a regularized manner.[44,45] In other words, we employ a diffuse representation of the ice–water interface using variable c that is a function of $\boldsymbol{x}$ and t:

$$c = c(\boldsymbol{x}, t) \text{ with } \begin{cases} c = 0 : & \text{completely frozen,} \\ c = 1 : & \text{completely unfrozen,} \\ c \in (0, 1) : & \text{diffuse ice-water interface,} \end{cases} \tag{5}$$

which is the solution of the Allen–Cahn phase-field equation[39,40] that will be presented later in Section 3.1. Based on this setting, we consider the degree of saturation of water as an interpolation function of the phase-field c, that is, $S^w = S^w(c)$, that monotonically increases from 0 to 1 as

$$S^w(c) = c^3(10 - 15c + 6c^2), \tag{6}$$

which guarantees smooth variation of different material properties between ice and water and at the same time enables us to properly include the latent heat effect in the energy balance equation in Section 3.1.1. Note that the evolution of the phase-field variable c itself does not necessarily imply the ice-lens growth since both the homogeneously frozen region

and segregated ice can reach $c = 0$, regardless of the level of the effective stress or stored energy that drives the crack growth (Figure 1).

The second phase-field variable $d \in [0, 1]$ adopted in this study is a damage parameter that treats the sharp discontinuity as a diffusive crack via implicit function.[41–43,52] In particular, we have

$$d = d(\boldsymbol{x}, t) \text{ with } \begin{cases} d = 0 & : \text{intact}, \\ d = 1 & : \text{damaged}, \\ d \in (0, 1) & : \text{transition zone}, \end{cases} \tag{7}$$

to approximate the fracture surface area A_Γ as A_{Γ_d}, which is the volume integration of crack surface density $\Gamma_d(d, \nabla d)$ over a body $\mathcal{B}$, that is

$$A_\Gamma \approx A_{\Gamma_d} = \int_{\mathcal{B}} \Gamma_d(d, \nabla d) dV; \Gamma_d(d, \nabla d) = \frac{d^2}{2l_d} + \frac{l_d}{2}(\nabla d \cdot \nabla d), \tag{8}$$

where l_d is the length scale parameter that controls the size of the transition zone. In this case, the crack resistance force $\mathcal{R}_d$ can be expressed as

$$\mathcal{R}_d = \frac{\partial W_d}{\partial d} - \nabla \cdot \left(\frac{\partial W_d}{\partial \nabla d} \right); W_d = \mathcal{G}_d \Gamma_d (d, \nabla d), \tag{9}$$

where $\mathcal{G}_d$ is the critical energy release rate that quantifies the resistance to cracking. As hinted in Figure 1, in order to guarantee crack irreversibility, the thermodynamic restriction $\dot{\Gamma}_d \geq 0$ must be satisfied[42,53–55] unlike the reversible freezing and thawing process. In other words, we require non-negative crack driving force $\mathcal{F}_d$ based on the microforce balance. Among multiple options, this study adopts the most widely used quadratic degradation function $g_d(d) = (1 - d)^2$ following[53], that reduces the thermodynamic restriction into $\dot{d} \geq 0$[56,57] and satisfies the following conditions:

$$g_d(0) = 1; g_d(1) = 0; \frac{\partial g_d(1)}{\partial d} = 0; \frac{\partial g_d(d)}{\partial d} \leq 0 \text{for} d \in [0, 1]. \tag{10}$$

Based on this setting, we define an indicator function $\chi^i \in [0, 1]$ for the segregated ice inside the freezing-induced fracture as follows:

$$\chi^i(c, d) = [1 - S^w(c)][1 - g_d(d)], \tag{11}$$

such that $\chi^i = 1$ implies the formation of the ice lens, which is different from the in-pore crystallization of the ice-phase constituent.

2.3 | Effective stress principle

Leveraging the similarities between freezing/thawing and drying/wetting processes, Miller and co-workers[19–21,51] proposed the concept of neutral stress that partitions the net pore pressure $\bar{p}$ into the pore water and pore ice pressures (p_w and p_i), respectively:

$$\bar{p} = S^w(c) p_w + [1 - S^w(c)] p_i. \tag{12}$$

Clearly, Equation (12) alone cannot capture the deviatoric stress induced by the deformation of the ice lens. Previous efforts on modeling frozen soil often relies on an extension of critical state theory that evolves the yield function according to the degree of saturation of ice (and therefore introduces the dependence of the tensile and shear strength on the presence of ice).[33,35] However, this treatment is not sufficient to consider the soil that may become brittle at low temperature due to the low moisture content and the influence of ice lens on the elasticity. Hence, this study extends Miller's approach into a phase-field framework by decomposing the effective stress tensor $\bar{\boldsymbol{\sigma}}'$ into two partial stresses for the solid and ice lens via

the damage phase field doubled as a weighting function, that is

$$\bar{\boldsymbol{\sigma}}' = g_d(d)\boldsymbol{\sigma}'_{\text{int}} + [1 - g_d(d)]\boldsymbol{\sigma}'_{\text{dam}} \tag{13}$$

where the second term on the right hand side of Equation (13) depends on the saturation $S^w(c)$. Specifically, the effective stress contribution from the solid skeleton $\boldsymbol{\sigma}'_{\text{int}}$ degrades due to the damage when the ice lens grows, but may also evolve by the change of $\boldsymbol{\sigma}'_{\text{dam}}$ in the presence of ice lens [for instance, see Equation (29) in Section 3.2]. From a physical point of view, we propose Equation (13) based on the assumption that there is no relative motion between the solid skeleton and the ice lens in the sense that the ice lenses cannot be squeezed out from the host matrix, which also has a benefit of ensuring continuous displacement field. Similar models that capture the constituent responses of porous media consisting of multiple solid constituents can also be found in Borja et al.[58] In addition, this study also considers the volumetric expansion due to the phase transition from water to ice while neglecting the thermal expansion or contraction of each phase constituent. Specifically, we incorporate an additional term for the total Cauchy stress tensor $\boldsymbol{\sigma}$ that describes phase-transition-induced volumetric expansion, which stems from the Helmholtz free energy functions of the solid- and ice-phase constituents postulated in Refs.[59,60] Hence, similar to Refs.,[33,35] as a modification of the Bishop's equation, the total Cauchy stress tensor can be expressed as follows:

$$\boldsymbol{\sigma} = \bar{\boldsymbol{\sigma}}' - \bar{p}\boldsymbol{I} - \phi[1 - S^w(c)]\bar{\alpha}_v K_i \boldsymbol{I}, \tag{14}$$

where $\bar{\alpha}_v = g_d(d)\alpha_{v,\text{int}} + [1 - g_d(d)]\alpha_{v,\text{dam}}$ is the net volumetric expansion coefficient, which is influenced by the evolution of the fracture. In particular, we assume that the volumetric expansion coefficient of the ice lens $\alpha_{v,\text{dam}}$ is greater than that of the pore ice crystal $\alpha_{v,\text{int}}$ due to the degradation of the solid skeleton.

3 | MULTIPHASE-FIELD MICROPOROMECHANICS MODEL FOR PHASE-CHANGING POROUS MEDIA

This section presents the balance principles and constitutive laws that capture the thermo-hydro-mechanical behavior of the phase-changing porous media. We first introduce the coupled field equations that govern the heat transfer and the ice–water phase transition processes, which involve the latent heat effect. Unlike previous studies that model the phase transition of the pore fluid by using the semi-empirical approach, which links either the Gibbs–Thomson equation[34] or the Clausius–Clapeyron equation[33,35] with the van Genuchten curve,[61] we adopt the Allen–Cahn type phase-field model[39,40] with a driving force that depends both on the temperature and the damage. We then present microporomechanics and phase-field fracture models that complete the set of governing equations, which is not only capable of simulating freeze–thaw action but also the freezing-induced or hydraulically driven fractures. The implications of our model will be examined via numerical examples in Section 5.

3.1 | Thermally induced phase transition

3.1.1 | Heat transfer

Since underground freezing and thawing processes may span over long temporal scales, this study employs a single temperature field θ by assuming that all the phase constituents reach a local thermal equilibrium instantly.[57] We also neglect thermal convection by considering the case where the target material possesses low permeability. Let e denote the internal energy per unit volume and $\boldsymbol{q}$ the heat flux. Then, the energy balance of the entire mixture can be expressed as[57,62]

$$\dot{e} = -\nabla \cdot \boldsymbol{q} + \hat{r}; e = e^s + \sum_{\alpha=\{w,i\}} e^\alpha, \tag{15}$$

where $\hat{r}$ indicates the heat source/sink, $e^s = \rho^s c_s \theta$ and $e^\alpha = \rho^\alpha c_\alpha \theta$ are the partial energies for the solid- and fluid-phase constituents, respectively, while c_s and c_α are their heat capacities. Although the freezing temperature of water (melting temperature of ice) depends on the curved phase boundaries due to the intermolecular forces, that is, freezing point

depression,[63] for simplicity, we assume that the freezing temperature of water remains constant $\theta_m = 273.15$ K, so that the internal energy of the entire mixture e in Equation (15) can be rewritten as

$$e = \rho^s c_s \theta + (\rho^w c_w + \rho^i c_i)(\theta - \theta_m) + (\rho^w c_w + \rho^i c_i)\theta_m. \tag{16}$$

From the relations shown in Equations (1)–(3), substituting Equation (16) into Equation (15) yields the following:

$$(\rho^s c_s + \rho^w c_w + \rho^i c_i)\dot{\theta} + \phi[(\rho_w c_w - \rho_i c_i)(\theta - \theta_m) + \rho_i L_\theta]\dot{S}^w(c) + \nabla \cdot \boldsymbol{q} = \hat{r}, \tag{17}$$

where

$$L_\theta = \left(\frac{\rho_w}{\rho_i} c_w - c_i\right)\theta_m \tag{18}$$

is the latent heat of fusion which is set to be $L_\theta = 334$ kJ/kg for pure water.[33,44,64,65] Notice that the second term on the left-hand side of Equation (17) describes the energy associated with the phase change of the fluid phase constituent $\alpha = \{w, i\}$, which is responsible for the constant temperature during the transformation processes, that is, where c is changing with time since $\dot{S}^w(c) = \{\partial S^w(c)/\partial c\}\dot{c}$. For the constitutive model that describes the heat conduction, this study adopts Fourier's law where the heat flux can be written as the dot product between the effective thermal conductivity and the temperature gradient, that is

$$\boldsymbol{q} = -\left(\phi^s \kappa_s + \sum_{\alpha=\{w,i\}} \phi^\alpha \kappa_\alpha\right) \cdot \nabla\theta, \tag{19}$$

where κ_s and κ_α denote the intrinsic thermal conductivities of the solid- and fluid-phase constituents, respectively. This volume-averaged approach, however, is only valid for the case where all the phase constituents are connected in parallel. Although there exists alternative homogenization approaches such as Eshelby's equivalent inclusion method,[66–68] determination of correct effective thermal conductivity often requires knowledge of the pore geometry and topology.[67,69,70] Since the information is not always readily approachable, this extension will be considered in the future.

3.1.2 | Phase transition

By using the phase field variable c defined in Equation (5), we adopt the Allen–Cahn model that is often used to simulate dendrite growth or multiphase flow.[39,71,72] Following Boettinger et al.,[40] we consider one of the simplest forms of the Gibbs free energy functional Ψ_c:

$$\Psi_c = \int_{\mathcal{B}} \psi_c \, dV = \int_{\mathcal{B}} f_c(\theta, c) + \frac{\epsilon_c^2}{2}|\nabla c|^2 \, dV, \tag{20}$$

where $f_c(\theta, c)$ is the free energy density that couples the heat transport with the phase transition, while ϵ_c is the gradient energy coefficient. From Equation (20), we consider the evolution of the phase field c over time, which yields the well-known Allen–Cahn equation or time-dependent Ginzburg–Landau equation, that is

$$-\frac{1}{M_c}\dot{c} = \frac{\partial \psi_c}{\partial c} - \nabla \cdot \left(\frac{\partial \psi_c}{\partial \nabla c}\right) = \frac{\partial f_c}{\partial c} - \epsilon_c^2 \nabla^2 c, \tag{21}$$

where $\nabla^2(\bullet) = \nabla \cdot \nabla(\bullet)$ is the Laplacian operator and M_c is the mobility parameter. Since this study does not consider solute transport or any other chemical effects, we focus on the pure water–ice phase transition such that the free energy density $f_c(\theta, c)$ can be written as

$$f_c = W_c g_c(c) + \mathcal{F}_c(\theta) p_c(c), \tag{22}$$

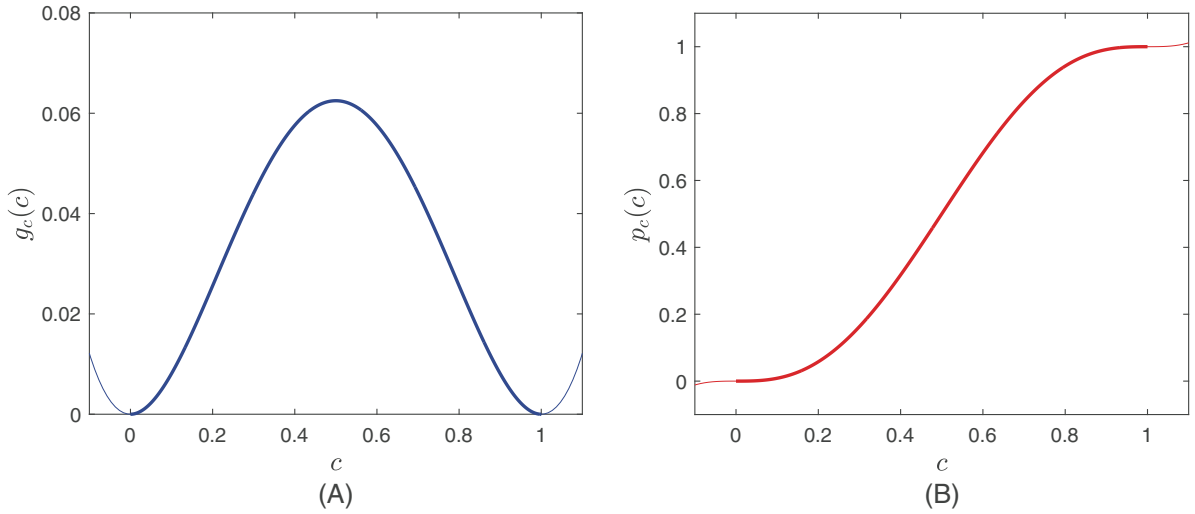

FIGURE 2 (A) The double well potential $g_c(c)$, and (B) the interpolation $p_c(c)$ functions. Thin colored curves correspond to the values outside the range of the phase field c

where $g_c(c) = c^2(1-c)^2$ is the double well potential (Figure 2A) that can be regarded as an energy barrier at the ice–water interface with the height of W_c, and $p_c(c) = S^w(c) = c^3(6c^2 - 15c + 10)$ is the interpolation function (Figure 2B) that ensures minima of the free energy density f_c at $c = 0$ and $c = 1$, respectively. The driving force $\mathcal{F}_c(\theta)$ that induces ice–water phase transition should describe the thermodynamically equilibrated state of water- and ice-phase constituents, which can be derived from the following relation[73]:

$$dp_i = \frac{\rho_i}{\rho_w} dp_w - \rho_i L_\theta \frac{d\theta}{\theta}. \tag{23}$$

Then, integrating Equation (23) yields the Clausius–Clapeyron equation

$$p_i - p_w = \left(\frac{\rho_i}{\rho_w} - 1\right) p_w - \rho_i L_\theta \ln \frac{\theta}{\theta_m}. \tag{24}$$

Equation (24) suggests that the surface tension develops along the ice–water interface, establishing the relation among water pressure (p_w), ice pressure (p_i), and temperature (θ). However, as pointed out in Nishimura et al.,[33] the ice–water-phase transition is mainly governed by the temperature while the influence of pressure on the ice saturation S^i is relatively minor. Hence, for simplicity, we define the driving force $\mathcal{F}_c(\theta)$ as an approximation of the pressure difference, by neglecting the effect of pore water pressure and adopt its first-order Taylor approximation following Boettinger et al.[40] as follows:

$$p_i - p_w \approx \mathcal{F}_c(\theta) = \rho_i L_\theta \left(1 - \frac{\theta}{\theta_m}\right). \tag{25}$$

As pointed out in Refs.,[40,44] since Equation (21) captures the evolution of the regularized ice–water interface, numerical parameters ϵ_c, W_c, and M_c can be related to the ice–water surface tension γ_{iw}, the interface thickness δ_c, and the kinetic coefficient ν_c as

$$\epsilon_c = \sqrt{6\gamma_{iw}\delta_c}; W_c = \frac{3\gamma_{iw}}{\delta_c}; M_c = \frac{\nu_c \theta_m}{6\rho_i L_\theta \delta_c}, \tag{26}$$

where the procedure that yields the relationships among the parameters is summarized in Appendix A. However, physical range of the width of the ice–water interface is at the atomic scale, that is, 10^{-10} m, which makes macro-scale simulations unfeasible.[45,74] In addition to the interfacial tension γ_{iw}, this study, therefore, treats the interface thickness δ_c and the gradient energy coefficient ϵ_c as input material parameters, since they could be increased according to the mesh size without significantly influencing the interface evolution.[44,75,76]

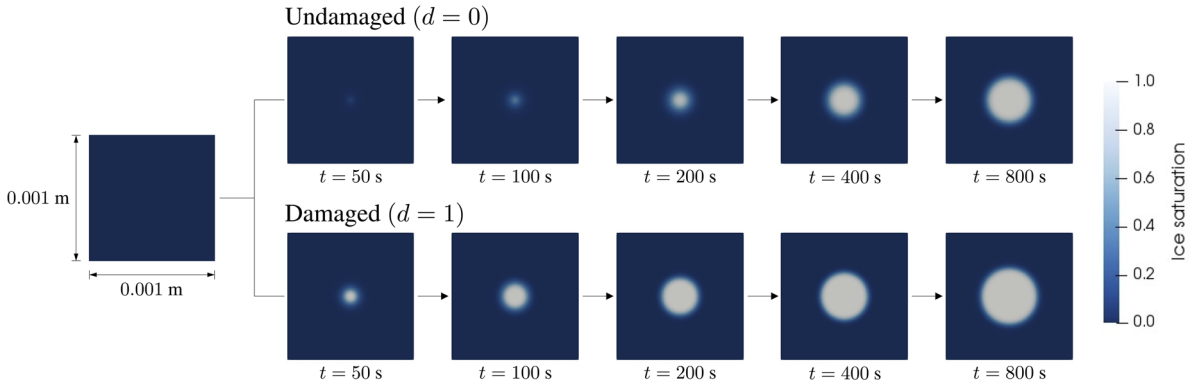

FIGURE 3 Different growth rates of the ice phases when a heat sink of $\hat{r} = -10^9$ W/m^3 is placed at a small region at the center with the area of $A_c = 10^{-10}$ m^2

Furthermore, since the existence of segregated ice governs the heave rate of frozen soil,[36,77] this study considers different rates between homogeneous freezing and ice-lens growth. Specifically, while employing different volumetric expansion coefficients for the in-pore crystallization and the formation of ice lens [Equation (14)], we replace the driving force $\mathcal{F}_c(\theta)$ with $\mathcal{F}_c^*(\theta, d)$ that contains an additional term that describes the intense growth of ice lenses similar to the kinetic equation proposed by Espinosa et al.,[78] which is often used to model salt crystallization in porous media[54,79,80]:

$$\mathcal{F}_c^*(\theta, d) = \rho_i L_\theta \left(1 - \frac{\theta}{\theta_m}\right) + [1 - g_d(d)] K_c^* \left(1 - \frac{\theta}{\theta_m}\right)^{g_c^*}, \tag{27}$$

where $K_c^* > 0$ and $g_c^* > 0$ are the kinetic parameters. The effect of the additional term in Equation (27) is illustrated in Figure 3, where we simulate the water–ice-phase transition by placing a heat sink at the center while the kinetic parameters are set to be $K_c^* = 5.0$ GPa and $g_c^* = 1.2$. By considering two different cases where the entire 1 mm^2 large water-saturated square domain remains intact and is completely damaged, Figure 3 shows that the modified driving force $\mathcal{F}_c^*$ is capable of capturing different growth rates depending on the damage parameter d.

3.2 | Freezing-induced fracture in microporoelastic medium

3.2.1 | Microporomechanics of the phase-changing porous medium

Focusing on the ice-lens formation that involves a long period of time up to annual scales,[81,82] this study neglects the inertial effects such that the balance of linear momentum for the three-phase mixture can be written as

$$\nabla \cdot \boldsymbol{\sigma} + \rho \boldsymbol{g} = \mathbf{0}. \tag{28}$$

Based on the observation that geological materials remain brittle at a low temperature,[83,84] we assume that the evolution of the damage parameter d replicates the mechanism of brittle fracture. In this case, undamaged effective stress $\boldsymbol{\sigma}'_{\text{int}}$ can be considered linear elastic, while the stress tensor inside the damaged zone should remain $\boldsymbol{\sigma}'_{\text{dam}} = \mathbf{0}$ unless the temperature is below θ_m to form bulk ice. Moreover, since the ice flow with respect to the solid phase is negligible compared to that of water,[34,35] both $\boldsymbol{\sigma}'_{\text{int}}$ and $\boldsymbol{\sigma}'_{\text{dam}}$ can be related to the strain measure $\boldsymbol{\varepsilon} = (\nabla \boldsymbol{u} + \nabla \boldsymbol{u}^{\text{T}})/2$ by approximating $\dot{\boldsymbol{v}}_i \approx \mathbf{0}$. Given these considerations, we define the constitutive relations for $\boldsymbol{\sigma}'_{\text{int}}$ and $\boldsymbol{\sigma}'_{\text{dam}}$ as

$$\boldsymbol{\sigma}'_{\text{int}} = K\varepsilon^{\text{vol}}\boldsymbol{I} + 2G\boldsymbol{\varepsilon}^{\text{dev}}; \boldsymbol{\sigma}'_{\text{dam}} = [1 - S^w(c)](K_i\varepsilon^{\text{vol}}\boldsymbol{I} + 2G_i\boldsymbol{\varepsilon}^{\text{dev}}), \tag{29}$$

where $\varepsilon^{\text{vol}} = \text{tr}(\boldsymbol{\varepsilon})$ and $\boldsymbol{\varepsilon}^{\text{dev}} = \boldsymbol{\varepsilon} - (\varepsilon^{\text{vol}}/3)\boldsymbol{I}$, while K and K_i are the bulk moduli; and G and G_i are the shear moduli for the solid skeleton and the ice, respectively. Based on this approach, $\boldsymbol{\sigma}'_{\text{dam}}$ can be interpreted as a developed stress due to the ice-lens growth, since it not only depends on the fracturing process but also on the state of the fluid phase.

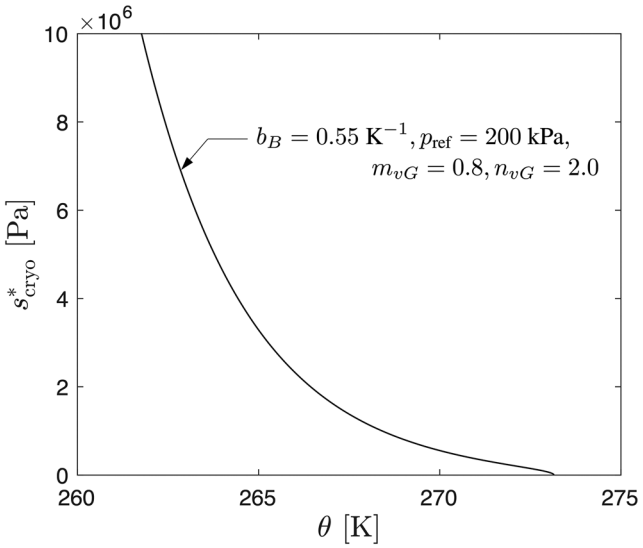

FIGURE 4 Freezing characteristic function [Equation (31)] used in this study

The net pore pressure $\bar{p}$, on the other hand, is a driver of deformation and fracture due to the formation of ice crystal that exerts significant excess pressure on the premelted water film. This pressure is referred to as cryo-suction s_{cryo} that induces the ice pressure p_i to be far greater than the water pressure p_w. As shown in Equations (12) and (24), the net pore pressure can be rewritten as $\bar{p} = [1 - S^w(c)]s_{\text{cryo}} - p_w$, while $s_{\text{cryo}} = p_i - p_w$ can be determined based upon the Clausius–Clapeyron equation. In practice, however, the Clausius–Clapeyron equation is typically replaced by an empirical model, such as the exponential[85] or the van Genuchten[61] curves, which is considered to be more accurate, since freezing retention characteristics are affected by both the pore size distribution and the ice–water interfacial tension[86–89]:

$$S^{w*} = \exp\left(b_B\langle\theta - \theta_m\rangle_-\right); s^*_{\text{cryo}} = p_{\text{ref}}\left[\{S^w(c)\}^{-\frac{1}{m_{vG}}} - 1\right]^{\frac{1}{n_{vG}}}, \tag{30}$$

where b_B, p_{ref}, m_{vG}, and n_{vG} are empirical parameters while $\langle\bullet\rangle_\pm = (\bullet \pm |\bullet|)/2$ is the Macaulay bracket. Note that we use a superscripted symbol $*$ to indicate that the corresponding variables are empirically determined. Yet, these empirical models still yield unrealistic results in some cases. For example, the derivative of the exponential model possesses a discontinuity at the freezing temperature θ_m, while s^*_{cryo} approaches infinity if $S^w(c) \to 0$ if adopting the van Genuchten model. Hence, in this study, we combine the two models to obtain the freezing retention curve that bypasses such issues (Figure 4):

$$s^*_{\text{cryo}} = p_{\text{ref}}\left\{\left[\{\exp\left(b_B\langle\theta - \theta_m\rangle_-\right)\}\right]^{-\frac{1}{m_{vG}}} - 1\right\}^{\frac{1}{n_{vG}}}, \tag{31}$$

and we replace s_{cryo} with s^*_{cryo} for the net pore pressure such that: $\bar{p} = [1 - S^w(c)]s^*_{\text{cryo}} - p_w$. For all the numerical examples presented in Section 5, we adopt the same values used in Refs.[35,89]: $b_B = 0.55\ \text{K}^{-1}$, $p_{\text{ref}} = 200$ kPa, $m_{vG} = 0.8$, and $n_{vG} = 2.0$.

Recall Section 2 that our material of interest is a fluid-saturated phase-changing porous media. Thus, this study considers the balance of mass for three-phase constituents (i.e., solid, water, and ice) as follows:

$$\dot{\rho}^s + \rho^s\nabla\cdot\boldsymbol{v} = \dot{m}_s, \tag{32}$$

$$\dot{\rho}^w + \rho^w\nabla\cdot\boldsymbol{v} + \nabla\cdot\rho^w\tilde{\boldsymbol{v}}_w = \dot{m}_w, \tag{33}$$

$$\dot{\rho}^i + \rho^i\nabla\cdot\boldsymbol{v} + \nabla\cdot\rho^i\tilde{\boldsymbol{v}}_i = \dot{m}_i, \tag{34}$$

where $\dot{m}_s$, $\dot{m}_w$, and $\dot{m}_i$ indicate the mass production rate for each phase constituent.[34,35,54] Here, we assume that only the water- and ice-phase constituents exchange mass among constituents (i.e., $\dot{m}_s = 0$ and $\dot{m}_w = -\dot{m}_i$). Hence, summation of Equations (33) and (34) yields

$$\dot{\phi}\{S^w(c)\rho_w + [1 - S^w(c)]\rho_i\} + \phi\dot{S}^w(c)(\rho_w - \rho_i) + \phi\{S^w(c)\rho_w + [1 - S^w(c)]\rho_i\}\nabla \cdot \boldsymbol{v} + \nabla \cdot \rho^w \tilde{\boldsymbol{v}}_w = 0, \tag{35}$$

since $\tilde{\boldsymbol{v}}_i \approx \boldsymbol{0}$, while Equation (32) can be rewritten as

$$\dot{\phi} = (1 - \phi)\nabla \cdot \boldsymbol{v}. \tag{36}$$

Substituting Equation (36) into Equation (35) yields the mass balance equation for the three-phase mixture:

$$\phi\dot{S}^w(c)(\rho_w - \rho_i) + \{S^w(c)\rho_w + [1 - S^w(c)]\rho_i\}\nabla \cdot \boldsymbol{v} + \nabla \cdot \rho^w \tilde{\boldsymbol{v}}_w = 0. \tag{37}$$

In this study, we focus on the case where the water flow inside both the porous matrix and the fracture obeys the generalized Darcy's law while considering the pore blockage due to the water–ice-phase transition.[90–92] In other words, we adopt the following constitutive relation between $\tilde{\boldsymbol{v}}_w$ and p_w:

$$\boldsymbol{w}_w = -\frac{k_r \boldsymbol{k}}{\mu_w}(\nabla p_w - \rho_w \boldsymbol{g}), \tag{38}$$

where $\boldsymbol{w}_w = \phi\tilde{\boldsymbol{v}}_w$ is Darcy's velocity, $\boldsymbol{k}$ is the permeability tensor, μ_w is the water viscosity, and k_r is the saturation dependent relative permeability:

$$k_r = S^w(c)^{1/2}\left\{1 - \left[1 - S^w(c)^{1/m_{vG}}\right]^{m_{vG}}\right\}^2. \tag{39}$$

Remark 1. Note that the linear elasticity model in Equation (29) is insufficient to accurately predict the elastoplastic behaviors during the thawing. A more comprehensive approach to capture the thawing process must take account of the healing of the soil (e.g., Eigenbrod[93]), the evolution of the hydraulic conductivity, the changes of the compressibility due to the reduction of over-consolidation ratio due to the effective stress built up during the thawing, as well as the geometric nonlinear due to the substantial settlement of the soil.[33,35,94,95] Incorporating these extensions with the phase-field ice-lens model will be considered in the future but is out of the scope of this study.

3.2.2 | Damage evolution

Following Hyoung Suk,[57] this study interprets cracking as the fracture of the solid skeleton. In other words, we define the crack driving force $\mathcal{F}_d \geq 0$ as

$$\mathcal{F}_d = -\frac{\partial g_d(d)}{\partial d}\psi'_{\text{int}}; \psi'_{\text{int}} = \frac{1}{2}K(\varepsilon^{\text{vol}})^2 + G(\boldsymbol{\varepsilon}^{\text{dev}} : \boldsymbol{\varepsilon}^{\text{dev}}), \tag{40}$$

such that the damage evolution equation can be obtained from the balance between the crack driving force $\mathcal{F}_d$ and the crack resistance $\mathcal{R}_d$[57,96,97]:

$$\mathcal{R}_d - \mathcal{F}_d = \frac{\partial g_d(d)}{\partial d}\psi'_{\text{int}} + \frac{\mathcal{G}_d}{l_d}(d - l_d^2\nabla^2 d) = 0. \tag{41}$$

Recall Section 2.2 that our choice of degradation function $g_d(d)$ reduces the thermodynamic restriction into $\dot{d} \geq 0$, which requires additional treatment to ensure monotonic crack growth. In this study, we adopt the same treatment used in Refs.[56,98] By considering the homogeneity $\nabla d = \boldsymbol{0}$, Equation (41) yields the following expression:

$$\dot{d} = \frac{2}{(1 + 2\mathcal{H})^2}\dot{\mathcal{H}} \geq 0; \mathcal{H} = \frac{\psi'^{+}_{\text{int}}}{\mathcal{G}_d/l_d}, \tag{42}$$

implying that non-negative $\dot{d}$ is guaranteed if $\dot{\mathcal{H}} \geq 0$. Here, notice that we adopt the volumetric-deviatoric splitting scheme proposed by Amor et al.[99] to avoid crack growth under compression. Specifically, we decompose the elastic strain energy into two parts, that is, $\psi'_{\text{int}} = \psi'^{+}_{\text{int}} + \psi'^{-}_{\text{int}}$,

$$\psi'_{\text{int}} = \frac{1}{2}K\langle\varepsilon^{\text{vol}}\rangle_+^2 + G(\boldsymbol{\varepsilon}^{\text{dev}} : \boldsymbol{\varepsilon}^{\text{dev}}); \psi'_{\text{int}} = \frac{1}{2}K\langle\varepsilon^{\text{vol}}\rangle_-^2, \tag{43}$$

and only degrade the expansive volumetric and deviatoric parts, while $\langle\bullet\rangle_\pm = (\bullet + |\bullet|)/2$. To ensure $\dot{\mathcal{H}} \geq 0$, as a simple remedy, we replace $\mathcal{H}$ with $\mathcal{H}^*$, which is defined as the pseudo-temporal maximum of normalized strain energy, while considering a critical value $\mathcal{H}_{\text{crit}}$ that restricts the crack to initiate above a threshold strain energy[56,100–102]:

$$\mathcal{H}^* = \max_{\tau\in[0,t]} \langle \mathcal{H} - \mathcal{H}_{\text{crit}}\rangle_+, \tag{44}$$

such that Equation (41) accordingly becomes

$$\frac{\partial g_d(d)}{\partial d}\mathcal{H}^* + (d - l_d^2\nabla^2 d) = 0. \tag{45}$$

For either partially or fully saturated soils, crack healing may occur during the thawing process. In specific, when ice lenses melt in a highly plastic clayey soil, cracks may heal due to the interactions between water molecules, whereas in a less cohesive soil, the precipitation of eroded particles may result in the clogging of cracks or cavities.[93,103,104] One possible approach to model the crack healing process is to allow crack driving force to decrease and incorporate a constitutive model that can capture the thaw-weakening process properly. For example, Ma and Sun[105] assumed that the healing process is activated when the material experiences volumetric compression, while the stiffness recovery rate becomes slower along the healing process. This extension is out of scope of this study, and hence, we assume that cracking is irreversible.

In order to model the fracture flow in a fluid-infiltrating porous media, we adopt the permeability enhancement approach that approximates the water flow inside the fracture as the flow between two parallel plates[106–109]:

$$\boldsymbol{k} = \boldsymbol{k}_{\text{mat}} + \boldsymbol{k}_d = k_{\text{mat}}\boldsymbol{I} + d^2 k_d(\boldsymbol{I} - \boldsymbol{n}_d \otimes \boldsymbol{n}_d), \tag{46}$$

where k_{mat} is the effective permeability of the undamaged matrix, $\boldsymbol{n}_d = \nabla d/\|\nabla d\|$ is the unit normal of crack surface, and $k_d = w_d^2/12$ describes the permeability enhancement due to the crack opening, which depends on the hydraulic aperture w_d based on the cubic law. However, freezing-induced fracture involves different situations where the pore ice crystal growth drives fracture, but at the same time blocks the pore that may hinder the water flow therein. Hence, we adopt the approach used in Choo et al.,[54] which assumes a linear relationship between the hydraulic aperture w_d and the water saturation $S^w(c)$:

$$w_d = S^w(c) l_\perp(\boldsymbol{n}_d \cdot \boldsymbol{\varepsilon} \cdot \boldsymbol{n}_d), \tag{47}$$

where $l_\perp$ is the characteristic length of a line element perpendicular to the fracture, which is often assumed to be equivalent to the mesh size.[106,110] Furthermore, by assuming that the crack opening leads to complete fragmentation of the solid matrix, we adopt the following relation for the porosity[57,111]:

$$\phi = 1 - g_d(d)(1 - \phi_0)(1 - \nabla \cdot \boldsymbol{u}), \tag{48}$$

such that the porosity approaches 1 if the solid skeleton is completely damaged.

Remark 2. Fragmentation and damage of the solid constituent may alter the microstructure of the solid skeleton. Nevertheless, if the constituent remains incompressible, then damage (e.g., split of incompressible particles) should not change the volume of the solid constituent constituted by a controlled mass and hence should not change the porosity. The only exception is when the fragmented particles eroded and flow inside the void space in which case a portion of solid mass is lost due to the damage (e.g., Refs. 112–114). In our case, we are using a regularized phase field to implicitly represent the crack surfaces and hence the dependence of damage in Equation (48) is used to capture the erosion. Note that a more

precise predictions may require a function difference from $g_d(d)$ to establish the relation between erosion and damage as well as the calculation of effective viscosity due to the erosion (see Pope[115]), which are out of the scope of this study but will be considered in the future.

4 | FINITE ELEMENT IMPLEMENTATION

This section presents a finite element discretization of the set of governing equations described in Section 3, and the solution strategy for the resulting discrete system. We first formulate the weak form of the field equations by following the standard weighted residual procedure. In specific, we adopt the Taylor–Hood element for the displacement and pore water pressure fields, while employing linear interpolation functions for all other variables in order to remove spurious oscillations. We then describe the operator split solution scheme that separately updates $\{\theta, c\}$ and $\{\boldsymbol{u}, p_w\}$, while the damage parameter d is updated in a staggered manner for numerical robustness.

4.1 | Galerkin form

Let domain $\mathcal{B}$ possesses boundary surface $\partial\mathcal{B}$ composed of Dirichlet boundaries (displacement $\partial\mathcal{B}_u$, pore water pressure $\partial\mathcal{B}_p$, and temperature $\partial\mathcal{B}_\theta$) and Neumann boundaries (traction $\partial\mathcal{B}_t$, water mass flux $\partial\mathcal{B}_w$, and heat flux $\partial\mathcal{B}_q$) that satisfies

$$\partial\mathcal{B} = \overline{\partial\mathcal{B}_u \cup \partial\mathcal{B}_t} = \overline{\partial\mathcal{B}_p \cup \partial\mathcal{B}_w} = \overline{\partial\mathcal{B}_\theta \cup \partial\mathcal{B}_q}; \emptyset = \partial\mathcal{B}_u \cap \partial\mathcal{B}_t = \partial\mathcal{B}_p \cap \partial\mathcal{B}_w = \partial\mathcal{B}_\theta \cap \partial\mathcal{B}_q. \tag{49}$$

Then, the prescribed boundary conditions can be specified as

$$\begin{cases} \boldsymbol{u} = \widehat{\boldsymbol{u}} & \text{on } \partial\mathcal{B}_u, \\ p_w = \widehat{p}_w & \text{on } \partial\mathcal{B}_p, \\ \theta = \widehat{\theta} & \text{on } \partial\mathcal{B}_\theta, \end{cases}; \begin{cases} \boldsymbol{\sigma}\cdot\boldsymbol{n} = \widehat{\boldsymbol{t}} & \text{on } \partial\mathcal{B}_t, \\ -\boldsymbol{w}_w\cdot\boldsymbol{n} = \widehat{w}_w & \text{on } \partial\mathcal{B}_w, \\ -\boldsymbol{q}\cdot\boldsymbol{n} = \widehat{q} & \text{on } \partial\mathcal{B}_q, \end{cases} \tag{50}$$

where $\boldsymbol{n}$ is the outward-oriented unit normal on the boundary surface $\partial\mathcal{B}$. Meanwhile, the following boundary conditions on $\partial\mathcal{B}$ are prescribed for the phase fields c and d:

$$\nabla c\cdot\boldsymbol{n} = 0; \nabla d\cdot\boldsymbol{n} = 0. \tag{51}$$

For model closure, the initial conditions for the primary unknowns $\{\boldsymbol{u}, p_w, \theta, c, d\}$ are imposed as

$$\boldsymbol{u} = \boldsymbol{u}_0; p_w = p_{w0}; \theta = \theta_0; c = c_0; d = d_0, \tag{52}$$

at time $t = 0$. We also define the trial spaces V_u, V_p, V_θ, V_c, and V_d for the solution variables as

$$\begin{aligned} V_u &= \left\{ \boldsymbol{u} : \mathcal{B} \to \mathbb{R}^3 \mid \boldsymbol{u} \in [H^1(\mathcal{B})]^3,\ \boldsymbol{u}|_{\partial\mathcal{B}_u} = \hat{\boldsymbol{u}} \right\}, \\ V_p &= \left\{ p_w : \mathcal{B} \to \mathbb{R} \mid p_w \in H^1(\mathcal{B}),\ p_w|_{\partial\mathcal{B}_p} = \hat{p}_w \right\}, \\ V_\theta &= \left\{ \theta : \mathcal{B} \to \mathbb{R} \mid \theta \in H^1(\mathcal{B}),\ \theta|_{\partial\mathcal{B}_\theta} = \hat{\theta} \right\}, \\ V_c &= \left\{ c : \mathcal{B} \to \mathbb{R} \mid c \in H^1(\mathcal{B}) \right\}, \\ V_d &= \left\{ d : \mathcal{B} \to \mathbb{R} \mid d \in H^1(\mathcal{B}) \right\}, \end{aligned} \tag{53}$$

which is complimented by the admissible spaces:

$$V_\eta = \left\{ \boldsymbol{\eta} : \mathcal{B} \to \mathbb{R}^3 \mid \boldsymbol{\eta} \in [H^1(\mathcal{B})]^3,\ \boldsymbol{\eta}|_{\partial\mathcal{B}_u} = \mathbf{0} \right\},$$
$$V_\xi = \left\{ \xi : \mathcal{B} \to \mathbb{R} \mid \xi \in H^1(\mathcal{B}),\ \xi\big|_{\partial\mathcal{B}_p} = 0 \right\},$$
$$V_\zeta = \left\{ \zeta : \mathcal{B} \to \mathbb{R} \mid \zeta \in H^1(\mathcal{B}),\ \zeta\big|_{\partial\mathcal{B}_\theta} = 0 \right\},$$
$$V_\gamma = \left\{ \gamma : \mathcal{B} \to \mathbb{R} \mid \gamma \in H^1(\mathcal{B}) \right\},$$
$$V_\omega = \left\{ \omega : \mathcal{B} \to \mathbb{R} \mid \omega \in H^1(\mathcal{B}) \right\}, \tag{54}$$

where H^1 indicates the Sobolev space of order 1. By applying the standard weighted residual procedure, the weak statements for Equations (17), (21), (28), (37), and (45) are to: find $\{\boldsymbol{u}, p_w, \theta, c, d\} \in V_u \times V_p \times V_\theta \times V_c \times V_d$ such that for all $\{\boldsymbol{\eta}, \xi, \zeta, \gamma, \omega\} \in V_\eta \times V_\xi \times V_\zeta \times V_\gamma \times V_\omega$,

$$G_u = G_p = G_\theta = G_c = G_d = 0, \tag{55}$$

where

$$G_u = \int_{\mathcal{B}} \nabla\boldsymbol{\eta} : \boldsymbol{\sigma}\, dV - \int_{\mathcal{B}} \boldsymbol{\eta} \cdot \rho\boldsymbol{g}\, dV - \int_{\partial\mathcal{B}_t} \boldsymbol{\eta} \cdot \hat{\boldsymbol{t}}\, d\Gamma = 0, \tag{56}$$

$$G_p = \int_{\mathcal{B}} \xi \left[\phi \dot{S}^w(c)(\rho_w - \rho_i)\right] dV + \int_{\mathcal{B}} \xi\{S^w(c)\rho_w + [1 - S^w(c)]\rho_i\}\nabla \cdot \boldsymbol{v}\, dV$$
$$- \int_{\mathcal{B}} \nabla\xi \cdot (\rho_w \boldsymbol{w}_w)\, dV - \int_{\partial\mathcal{B}_w} \xi(\rho_w \hat{\boldsymbol{w}}_w)\, d\Gamma = 0, \tag{57}$$

$$G_\theta = \int_{\mathcal{B}} \zeta(\rho^s c_s + \rho^w c_w + \rho^i c_i)\dot{\theta}\, dV + \int_{\mathcal{B}} \zeta\left\{\phi[(\rho_w c_w - \rho_i c_i)(\theta - \theta_m) + \rho_i L_\theta]\dot{S}^w(c)\right\} dV$$
$$- \int_{\mathcal{B}} \nabla\zeta \cdot \boldsymbol{q}\, dV - \int_{\mathcal{B}} \zeta\hat{r}\, dV - \int_{\partial\mathcal{B}_q} \zeta\hat{q}\, d\Gamma = 0, \tag{58}$$

$$G_c = \int_{\mathcal{B}} \gamma \frac{1}{M_c}\dot{c}\, dV + \int_{\mathcal{B}} \gamma \frac{\partial f_c}{\partial c}\, dV + \int_{\mathcal{B}} \nabla\gamma \cdot (\epsilon_c^2 \nabla c)\, dV = 0, \tag{59}$$

$$G_d = \int_{\mathcal{B}} \omega \frac{\partial g_d(d)}{\partial d}\mathcal{H}^*\, dV + \int_{\mathcal{B}} \omega d\, dV + \int_{\mathcal{B}} \nabla\omega \cdot (l_d^2 \nabla d)\, dV = 0. \tag{60}$$

4.2 | Operator-split solution strategy

Although one may consider different strategies to solve the coupled system of equations [Equations (56)–(60)], the solution strategy adopted in this study combines the staggered scheme[42] and the isothermal operator splitting scheme.[116,117] Specifically, we first update the damage field d via linear solver while the variables $\{\boldsymbol{u}, p_w, \theta, c\}$ are held fixed. We then apply the isothermal splitting solution scheme that iteratively solves the thermally induced phase transition problem to advance $\{\theta, c\}$, followed by a linear solver that updates $\{\boldsymbol{u}, p_w\}$ by solving an isothermal poromechanics problem,[57]

that is

$$\underbrace{\begin{bmatrix}\boldsymbol{u}_{\mathrm{n}}\\ p_{w,\mathrm{n}}\\ \theta_{\mathrm{n}}\\ c_{\mathrm{n}}\\ d_{\mathrm{n}}\end{bmatrix}\xrightarrow[\delta\boldsymbol{u}=\boldsymbol{0},\,\delta p_w=0,\,\delta\theta=0,\,\delta c=0]{G_d=0}\begin{bmatrix}\boldsymbol{u}_{\mathrm{n}}\\ p_{w,\mathrm{n}}\\ \theta_{\mathrm{n}}\\ c_{\mathrm{n}}\\ d_{\mathrm{n+1}}\end{bmatrix}}_{\text{Linear solver}}\overbrace{\underbrace{\xrightarrow[\delta\boldsymbol{u}=\boldsymbol{0},\,\delta p_w=0,\,\delta d=0]{G_\theta=G_c=0}\begin{bmatrix}\boldsymbol{u}_{\mathrm{n}}\\ p_{w,\mathrm{n}}\\ \theta_{\mathrm{n+1}}\\ c_{\mathrm{n+1}}\\ d_{\mathrm{n+1}}\end{bmatrix}\xrightarrow[\delta\theta=0,\,\delta c=0,\,\delta d=0]{G_u=G_p=0}\begin{bmatrix}\boldsymbol{u}_{\mathrm{n+1}}\\ p_{w,\mathrm{n+1}}\\ \theta_{\mathrm{n+1}}\\ c_{\mathrm{n+1}}\\ d_{\mathrm{n+1}}\end{bmatrix}}_{\text{Linear solver}}}^{\text{Iterative solver}},\tag{61}$$

where we adopt an implicit backward Euler time integration scheme. The implementation of the model including the finite element discretization and the solution scheme relies on the finite element package `FEniCS`[118–120] with `PETSc` scientific computational toolkit.[121]

5 | NUMERICAL EXAMPLES

This section presents three sets of numerical examples to verify (Section 5.1), validate (Section 5.2), and showcase (Sections 5.3 and 5.4) the capacity of the proposed model. Since the evolution of two-phase fields c and d requires a fine mesh to capture their sharp gradients, we limit our attention to one- or two-dimensional simulations while considering the diffusion coefficient ϵ_c as an individual input parameter independent to the interface thickness δ_c, which may additionally reduce the computational cost.[45,122] We first present two examples that simulate the latent heat effect and 1d consolidation to verify the implementation of our proposed model. As a validation exercise, we perform numerical experiments that replicate the physical experiments conducted by Feng et al.,[123] which studies the homogeneous freezing of a phase change material (PCM) embedded in metal foams. We then showcase the performance of the computational model for simulating the ice-lens formation and the thermo-hydro-mechanical processes in geomaterials undergoing freeze–thaw cycle, and also its capacity to simulate nonplanar ice-lens growth that follows the crack trajectory.

5.1 | Verification exercises: latent heat effect and 1d consolidation

Our first example simulates one-dimensional freezing of water-saturated porous media to investigate the phase transition of the fluid phase $\alpha = \{w, i\}$ and the involved latent heat effect. By comparing the results against the models presented by Lackner et al.[124] and Sweidan et al.,[45] this example serves as a verification exercise that ensures the robust implementation of the heat transfer model involving phase transition [i.e., Equations (58) and (59)]. Hence, this example considers a rigid solid matrix while neglecting the fluid flow, following Lackner et al.[124] As illustrated in Figure 5A, the problem domain is a fully saturated rectangular specimen with a height of 0.09 m and a width of 0.41 m. While the initial temperature of the entire specimen is set to be $\theta_0 = 283.15$ K, the specimen is subjected to freezing with a constant heat flux of $\hat{q} = 100$ W/m^2 on the top surface, whereas all other boundaries are thermally insulated. Here, we choose the same material properties used in Lackner et al.[124] and Sweidan et al.[45] as follows: $\phi_0 = 0.42$, $\rho_s = 2650$ kg/m^3, $\rho_w = 1000$ kg/m^3, $\rho_i = 913$ kg/m^3, $c_s = 740$ J/kg/K, $c_w = 4200$ J/kg/K, $c_i = 1900$ J/kg/K, $\kappa_s = 7.694$ W/m/K, $\kappa_w = 0.611$ W/m/K, and $\kappa_i = 2.222$ W/m/K. In addition, we set $v_c = 0.001$ m/s, $\gamma_c = 0.03$ J/m^2, $\delta_c = 0.005$ m, and $\epsilon_c = 1.25$ (J/m)$^{1/2}$ for the Allen–Cahn phase-field model, while we use the structured mesh with element size of $h_e = 0.6$ mm and choose the time step size of $\Delta t = 100$ s.

As shown in Figure 5B, measured temperatures at points A, B, and C during the simulation first linearly decrease due to the applied heat flux $\hat{q}$ until they reach the freezing temperature of $\theta_m = 273.15$ K. As soon as the phase transition starts, the freezing front propagates through the specimen while the release of the energy associated with the phase transition prevents the temperature decrease (i.e., latent heat effect). Once the phase change is complete, the temperature linearly decreases over time again since the heat transfer process is no longer affected by the latent heat. More importantly, a good agreement with the results reported in Refs.[45,124] verifies that our proposed model is capable of capturing the thermal behavior of the phase-changing porous media.

For the second verification exercise, we choose the classical Terzaghi's 1d consolidation problem since it possesses an analytical solution,[125] which can directly be compared with the results obtained via poromechanics model [Equations (56)

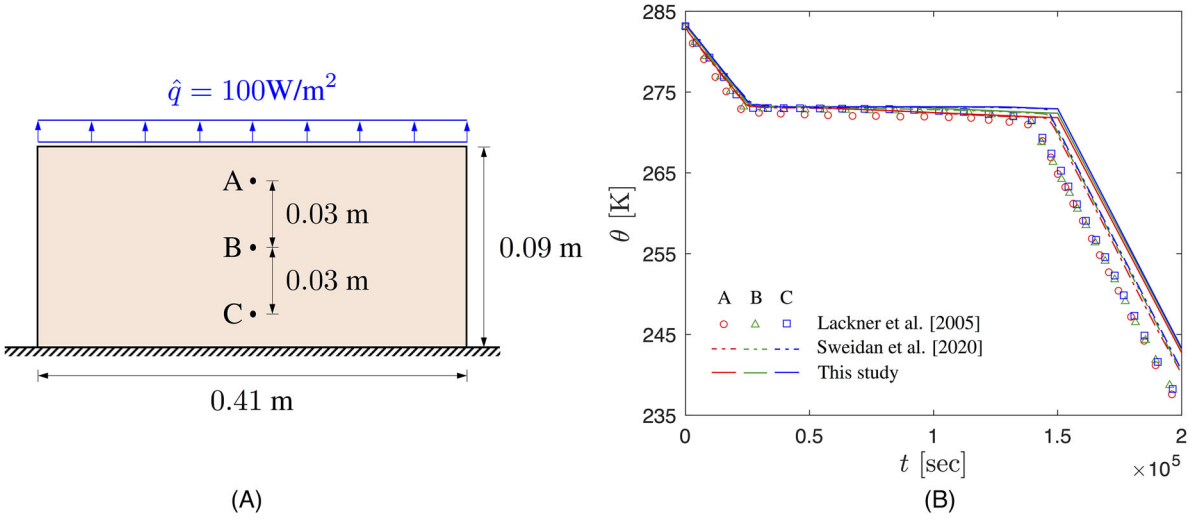

FIGURE 5 (A) Schematic of geometry and boundary conditions for the 1d freezing example; (B) temperature evolution at points A, B, and C

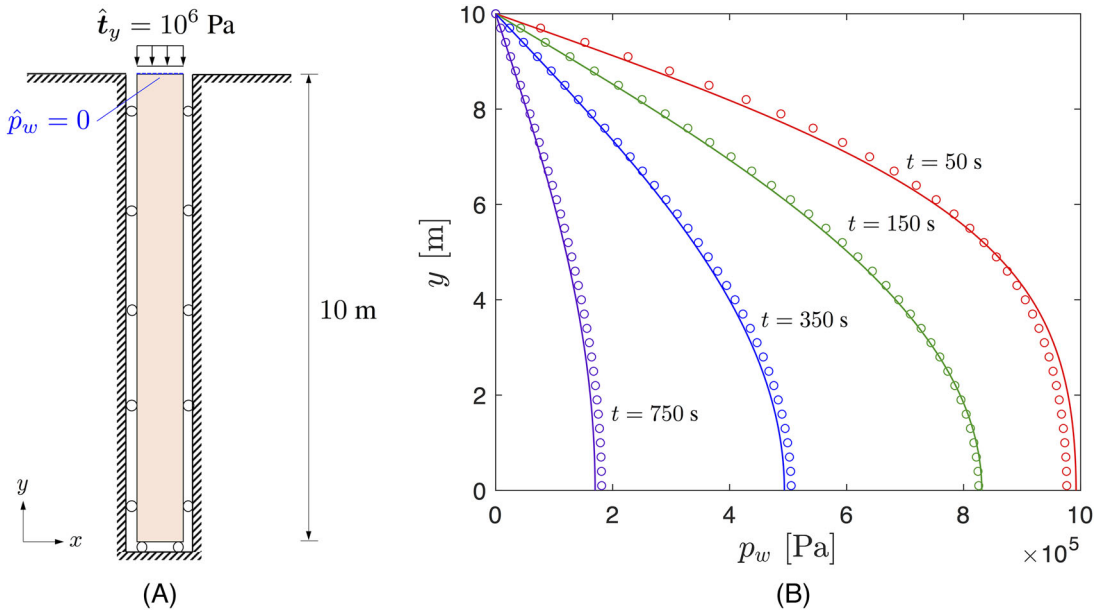

FIGURE 6 (A) Schematic of geometry and boundary conditions for Terzaghi's problem; (B) time-dependent pore water pressures along the height of the specimen

and (57)]. Our problem domain shown in Figure 6A consists of a 10-m high water-saturated linear elastic soil mass. While a 1-MPa compressive load $\boldsymbol{t}_y$ is imposed on the top surface, we replicate the single-drained condition by prescribing zero pore water pressure at the top ($\hat{p}_w = 0$) and a no-slip condition at the bottom. By assuming that the temperature of the soil column remains constant during the simulation ($\theta = 293.15$ K), we only focus on its hydro-mechanically coupled response while the material parameters are chosen as follows: $\phi_0 = 0.4$, $\rho_s = 2650$ kg/m^3, $\rho_w = 1000$ kg/m^3, $K = 66.67$ MPa, $G = 40$ MPa, $k_{\text{mat}} = 10^{-12}$ m^2, and $\mu_w = 10^{-3}$ Pa·s. Here, we choose $h_e = 0.1$ m and $\Delta t = 20$ s.

Figure 6B illustrates the pore water pressure profile during the simulation at $t = 50, 150, 350$, and 750 s. The results show that the applied mechanical load $\boldsymbol{t}_y$ builds up the pore water pressure, affecting the pore water to migrate towards the top surface, which leads to the dissipation of the excess pressure over time (i.e., consolidation). By comparing the simulation results (circular symbols) to the analytical solution (solid curves), Figure 6B verifies the reliability of our model to capture the hydro-mechanically coupled responses.

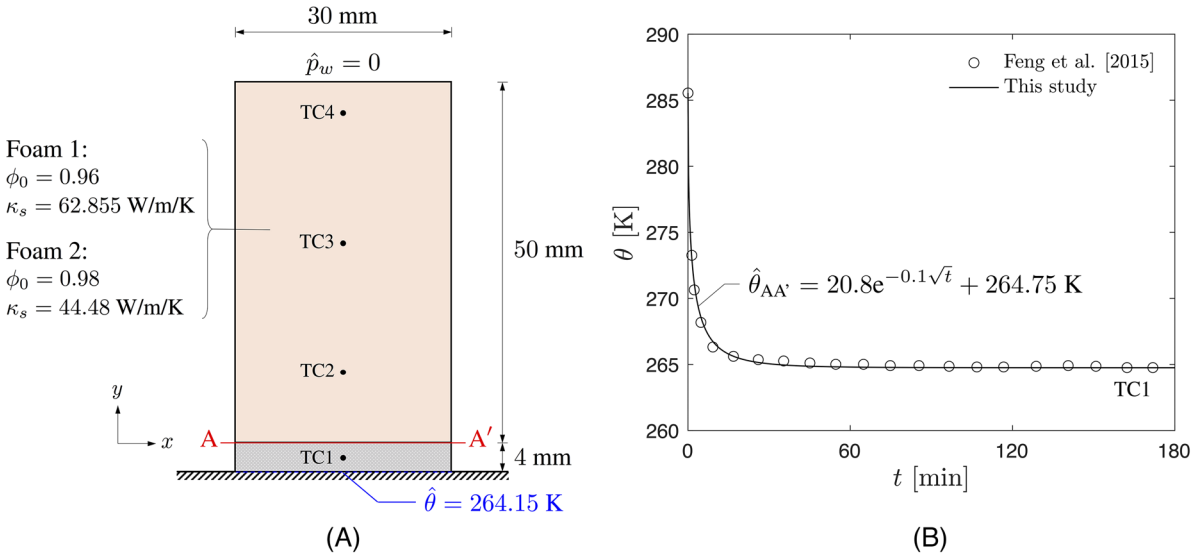

FIGURE 7 (A) Schematic of the experimental setup for the unidirectional freezing test conducted in Feng et al.[123]; (B) temperature boundary condition applied at the bottom surface of the copper foam (AA') for the numerical simulation

5.2 | Validation example: homogeneous freezing

This section compares the results obtained from the numerical simulation against the physical experiment conducted by Feng et al.[123]. This experiment is used as a benchmark since it considers the unidirectional freezing of distilled water filled in porous copper foams, which does not involve a fracturing process and yields a clear water–ice boundary layer due to the microstructural attributes of the host matrix. As schematically shown in Figure 7A, a 30-mm-wide, 50-mm-long water-saturated copper foam is mounted on a 4-mm-thick copper block. While the initial temperature is measured to be $\theta_0 = 285.55$ K, the experiment is performed by applying a constant temperature of $\hat{\theta} = 264.15$ K at the bottom part of the copper block at $t = 0$. Temperature measurements during the experiment are made by three thermocouples (TC2-TC4) located at 10, 28, and 46 mm from the bottom of the foam (AA'), whereas TC1 records the temperature of the block. For the numerical simulation, instead of considering the problem domain as a layered material, we only focus on the water-saturated copper foam and apply time-dependent Dirichlet boundary condition on AA' by using the temperature measured by TC1 (Figure 7B). We also assume an unlimited water supply from the top surface by imposing $\hat{p}_w = 0$ and applying a fixed boundary condition at the bottom part of the foam. Moreover, we consider two different types of copper foams (Foam 1 and Foam 2) with different initial porosity and thermal conductivity (Figure 7a). As summarized in Table 1, our numerical simulation directly adopts the same thermal properties compared to the physical experiment whereas the solid phase thermal conductivities of the foams are computed based upon the effective properties reported in Feng et al.[123] For all other material parameters that are not specified in Feng et al.,[123] we choose the properties that resemble those of the water-saturated copper foam. In this section, the Allen–Cahn parameters are chosen as: $\nu_c = 0.0001$ m/s, $\gamma_c = 0.065$ J/m^2, $\delta_c = 0.0001$ m, and $\epsilon_c = 0.75$ (J/m)$^{1/2}$, while adopting a structured mesh with $h_e = 2.5$ mm and $\Delta t = 60$ s.

Figure 8 illustrates the evolution of the freezing front within a water-saturated copper foam (Foam 2). In both the physical and numerical experiments, water freezing starts from the bottom (AA') and migrates towards the upper part of the foam over time, depending on the conductive heat transfer process. While it shows a qualitative agreement between the two, Figure 9 quantitatively confirms the validity of our model, where we use the circular symbols to indicate the experimental measurements whereas the solid curves denote the numerical results. As shown in Figure 9A, since Foam 1 possesses higher solidity (lower porosity) compared to Foam 2, the water–ice interface tends to grow relatively faster because it exhibits higher effective thermal conductivity. In addition, temperature variations illustrated in Figure 9B clearly show the interplay between the thermal boundary layer growth and the latent heat, resulting in a nonlinear evolution of the freezing front. Although has not been measured experimentally, we further investigate the time-dependent hydro-mechanical response of the specimen from the simulation results shown in Figure 10. Based on the freezing retention curve [Equation (31)] adopted in this study, positive suction starts to develop if $\theta < \theta_m$ while the region where $s^*_{\text{cryo}} > 0$ evolves over time following the same trajectory of that of the freezing front (Figure 10A). This process also involves a

TABLE 1 Material parameters for the validation exercise

Parameter	Description [Unit]	Value	Reference
ρ_s	Intrinsic solid mass density [kg/m^3]	7800.0	-
ρ_w	Intrinsic water mass density [kg/m^3]	1000.0	[123]
ρ_i	Intrinsic ice mass density [kg/m^3]	920.0	[123]
c_s	Specific heat of solid [J/kg/K]	0.385×10^3	-
c_w	Specific heat of water [J/kg/K]	4.216×10^3	[123]
c_i	Specific heat of ice [J/kg/K]	2.040×10^3	[123]
κ_s	Thermal conductivity of solid [W/m/K]	62.855, 44.48	[123]
κ_w	Thermal conductivity of water [W/m/K]	0.56	[123]
κ_i	Thermal conductivity of ice [W/m/K]	1.90	[123]
K	Bulk modulus of solid skeleton [Pa]	0.555×10^9	-
K_i	Bulk modulus of ice [Pa]	5.56×10^9	-
G	Shear modulus of solid skeleton [Pa]	0.185×10^9	-
G_i	Shear modulus of ice [Pa]	4.20×10^9	-
ϕ_0	Initial porosity [-]	0.96, 0.98	[123]
k_{mat}	Matrix permeability [m^2]	3.25×10^{-7}	-
μ_w	Viscosity of water [Pa·s]	1.0×10^{-3}	-
$\alpha_{v,\text{int}}$	Volumetric expansion coefficient [-]	5.0×10^{-3}	-

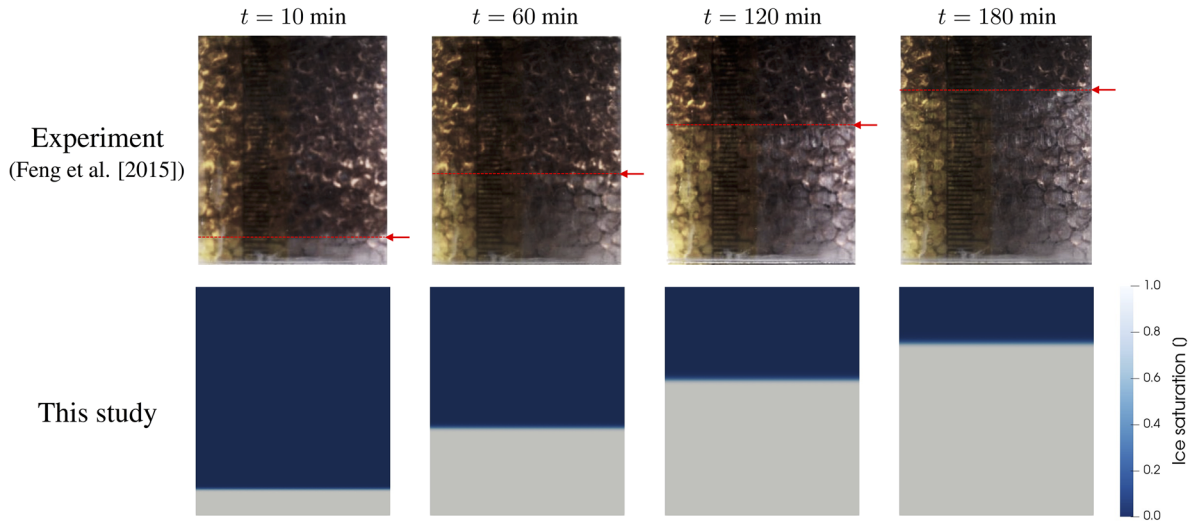

FIGURE 8 Comparison between the physical and numerical experiments on the evolution of the water–ice interface

volumetric expansion of the specimen that leads to an increase of the vertical displacement as shown in Figure 10B, due to the difference between water (ρ_w) and ice densities (ρ_i). Since our framework idealizes the material as a multiphase mixture of the solid-, water-, and ice-phase constituents, notice that relatively small displacement compared to the volume expansion due to the ice–water phase transition is because of the mechanical properties of the host matrix, which is less compressible compared to geological materials. It should be also noted that the freezing front always exhibits the largest vertical displacement, implying that the water migration towards the freezing front induced by the suction triggers the consolidation process above the frozen area, resulting in a small volumetric compression therein. This observation agrees with the explanation in Amato et al.[126] where the consolidation front of a frozen soil has been observed experimentally, which corroborates the applicability of our proposed model.

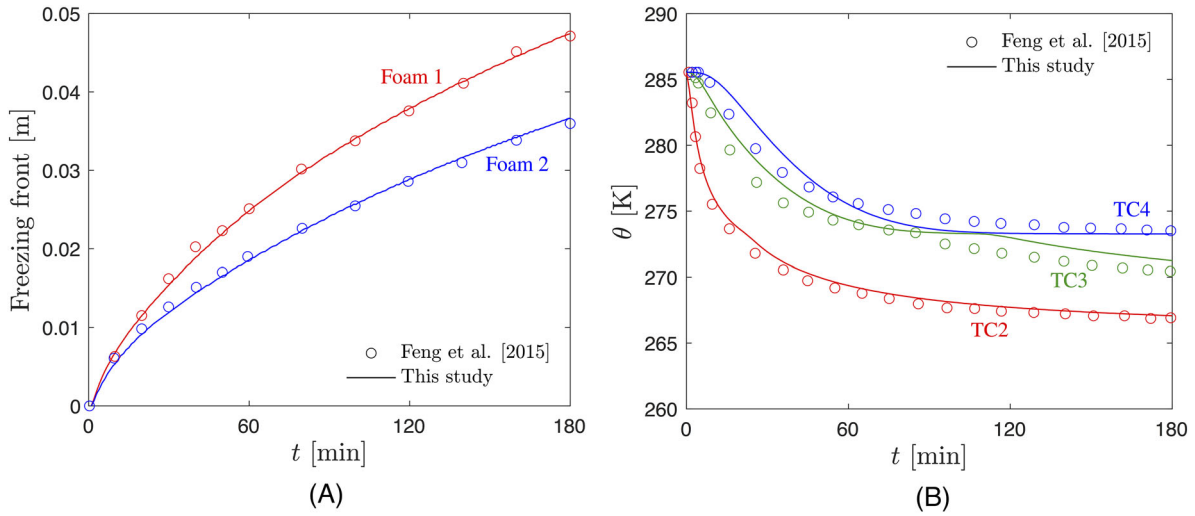

FIGURE 9 (A) Evolution of the freezing front over time; (B) temperature variation within Foam 2 measured from TC2, TC3, and TC4

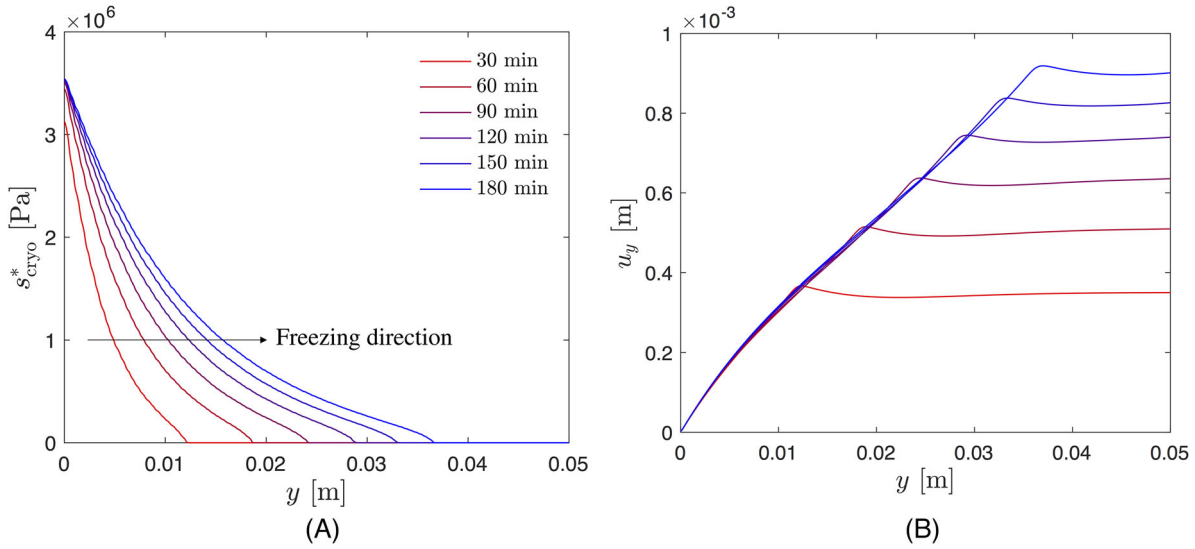

FIGURE 10 Hydro-mechanical response of Foam 2 subjected to freezing: (A) cryo-suction (s^*_{cryo}) and (B) vertical displacement (u_y) profiles

5.3 | Freeze–thaw action: multiple ice lens growth and thawing in heterogeneous soil

In this section, we showcase the capability of our proposed model by simulating the formation and melting of multiple ice lenses inside a heterogeneous clayey soil specimen. As illustrated in Figure 11A, the problem domain is 0.04-m wide and 0.1-m long soil column that possesses a random porosity profile along the vertical axis with a mean value of $\phi_{\text{ref}} = 0.4$ such that the specimen possesses layered microstructure. In addition, we introduce a set of heterogeneous material properties that solely depends on the spatial distribution of initial porosity ϕ_0. Specifically, we adopt a phenomenological model proposed by Uyanık[127] for the shear modulus G, while we use a power law for the critical energy release rate $\mathcal{G}_d$ similar to Kun & Sun, and Dunn et al. [108,128]:

$$G = \frac{3}{2}\left(\frac{1-2\nu}{1+\nu}\right)\exp\left[10(1-\phi_0)\right]\,[\text{MPa}];\mathcal{G}_d = \mathcal{G}_{d,\text{ref}}\left(\frac{1-\phi_0}{1-\phi_{\text{ref}}}\right)^{n_\phi}. \tag{62}$$

Here, we assume that the Poisson's ratio remains constant $\nu = 0.25$ throughout the entire domain while we set $\mathcal{G}_{d,\text{ref}} = 1.5$ N/m and $n_\phi = 50$. Based on this setting, we attempt to incorporate ice-lens initiation criterion proposed by Zhou and

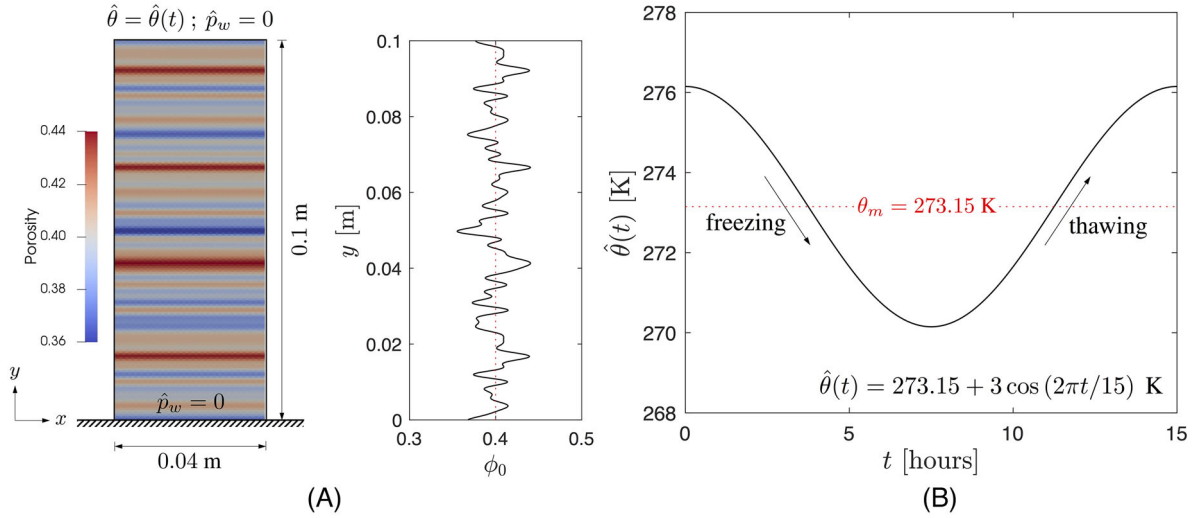

FIGURE 11 (A) Schematic of geometry and boundary conditions for the numerical freeze–thaw test; (B) temperature boundary condition applied at the top surface

TABLE 2 Material parameters for the numerical freeze-thaw test

Parameter	Description [Unit]	Value
ρ_s	Intrinsic solid mass density [kg/m^3]	2650.0
ρ_w	Intrinsic water mass density [kg/m^3]	1000.0
ρ_i	Intrinsic ice mass density [kg/m^3]	920.0
c_s	Specific heat of solid [J/kg/K]	0.75×10^3
c_w	Specific heat of water [J/kg/K]	4.20×10^3
c_i	Specific heat of ice [J/kg/K]	1.90×10^3
κ_s	Thermal conductivity of solid [W/m/K]	7.69
κ_w	Thermal conductivity of water [W/m/K]	0.56
κ_i	Thermal conductivity of ice [W/m/K]	2.25
K_i	Bulk modulus of ice [Pa]	5.56×10^9
G_i	Shear modulus of ice [Pa]	4.20×10^9
ϕ_{ref}	Reference porosity [–]	0.4
k_{mat}	Matrix permeability [m^2]	1.0×10^{-13}
μ_w	Viscosity of water [Pa·s]	1.0×10^{-3}
$\mathcal{G}_{d,\text{ref}}$	Reference critical energy release rate [N/m]	1.5
l_d	Regularization length scale parameter [m]	1.0×10^{-3}
$\mathcal{H}_{\text{crit}}$	Normalized threshold strain energy [–]	0.05
$\alpha_{v,\text{int}}$	Volumetric expansion coefficient (intact) [–]	5.0×10^{-3}
$\alpha_{v,\text{dam}}$	Volumetric expansion coefficient (damaged) [–]	80.0×10^{-3}
K_c^*	Kinetic parameter [Pa]	5.0×10^9
g_c^*	Kinetic parameter [–]	1.25

Li,[25] where a separation void ratio determines the positions of the ice lenses. For all other material properties that are homogeneous, as summarized in Table 2, we choose values similar to those of the clayey soil. It should be noted that we adopt $\alpha_{v,\text{dam}} = 0.08$, which is identical to the theoretical value of $1 - \rho_i/\rho_w$ for the expansion coefficient, whereas we set $\alpha_{v,\text{int}} = 0.005$ due to the existence of thin water film between the intact solid and the pore ice. Meanwhile, the parameters for the Allen–Cahn phase-field equation are chosen as: $\nu_c = 0.0001$ m/s, $\gamma_c = 0.065$ J/m^2, $\delta_c = 0.0001$ m, and $\epsilon_c = 1.0$ (J/m)$^{1/2}$, whereas we set $h_e = 0.5$ mm and $\Delta t = 60$ s.

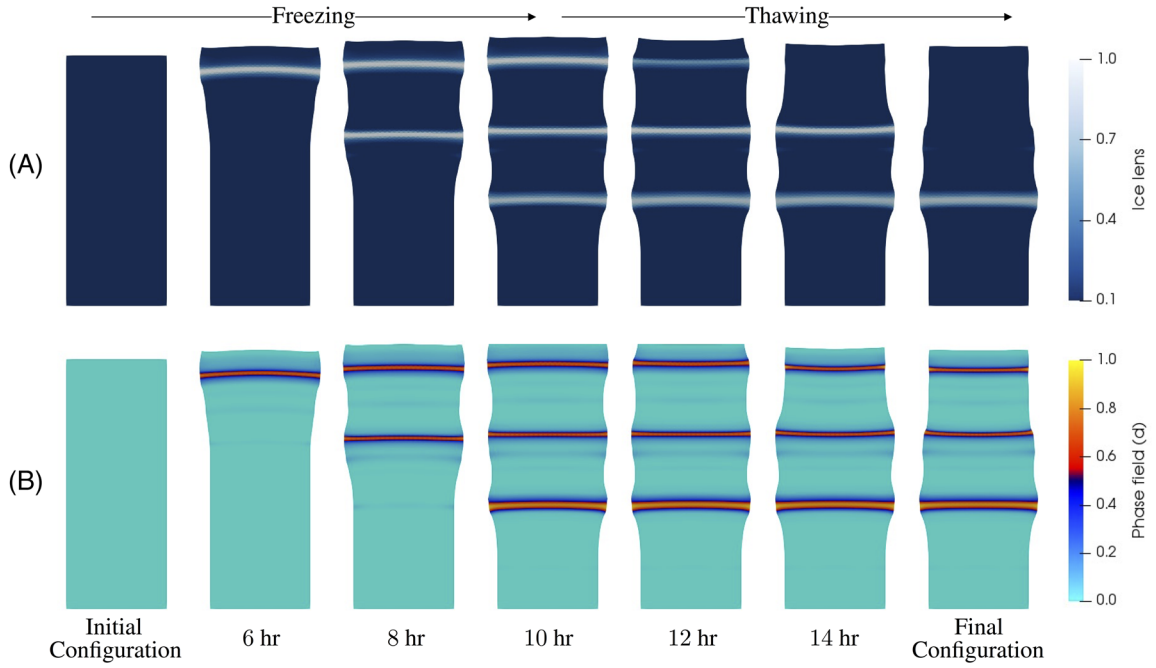

FIGURE 12 (A) Formation and melting of multiple ice lenses and (B) evolution of the fracture phase field d during the numerical freeze–thaw test

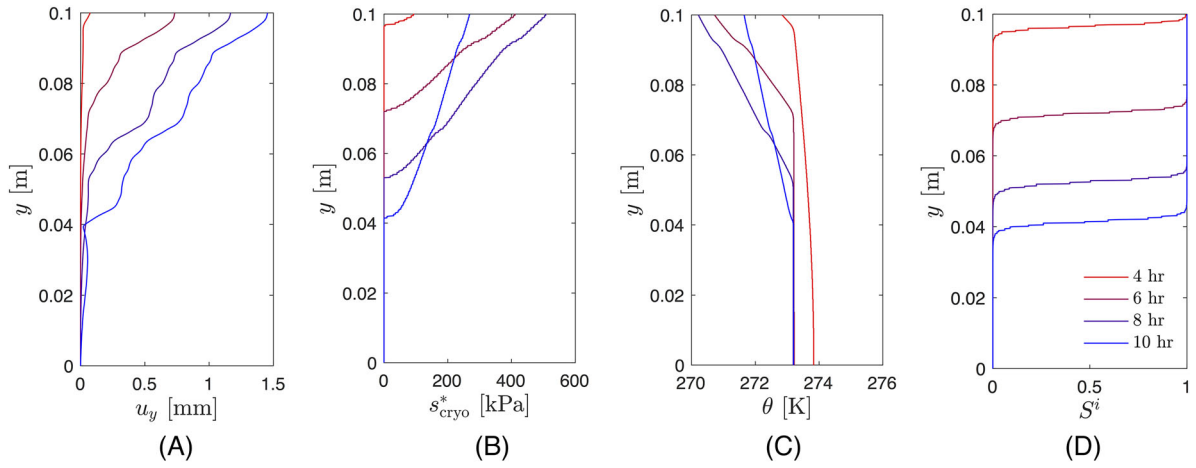

FIGURE 13 Thermo-hydro-mechanical response of the specimen during the freezing phase: (A) vertical displacement (u_y), (B) cryo-suction (s^*_{cryo}), (C) temperature (θ), and (D) ice saturation (S^i) profiles along the central axis

While we set the initial temperature as $\theta_0 = 276.15$ K, the numerical freeze–thaw test is performed by applying a time-dependent temperature boundary condition at the top, represented by a sinusoidal function. As shown in Figure 11B, the freezing process starts at $t = 3.75$ h and continues until the top surface temperature reaches the melting temperature of $\theta_m = 273.15$ K at $t = 11.25$ h, where the frozen soil begins to thaw. During the simulation, the bottom part of the specimen is held fixed while we prescribe zero pore water pressure boundaries ($\hat{p}_w = 0$) at both the top and the bottom surfaces. The left and right boundaries, on the other hand, are subjected to zero water mass flux and heat flux conditions. Based on this setting, the water is supplied from the bottom during the freezing phase, while the water expulsion towards the top surface during the melting phase leads to a thawing settlement of the specimen.

Figure 12 shows the formation and melting of multiple ice lenses and the evolution of the fracture phase field during the numerical freeze–thaw test. Here, we use a scaling factor of 5 while the color bar illustrated in Figure 12A represents the value of the indicator function χ^i defined in Equation (11). As illustrated in Figure 13, the water freezes from the top to the bottom during the freezing phase (3.75 h $\leq t \leq$ 11.25 h), which leads to the development of the cryo-suction and a

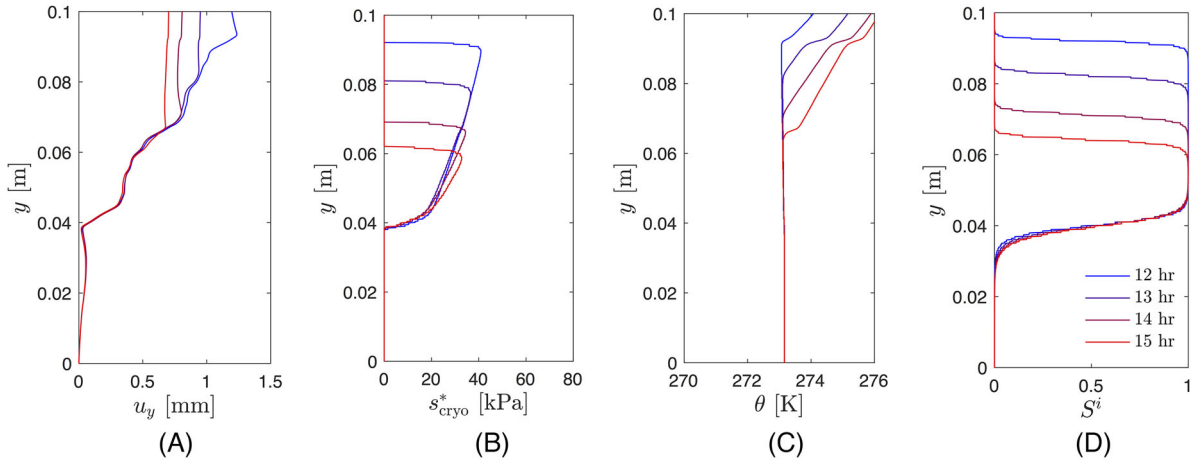

FIGURE 14 Thermo-hydro-mechanical response of the specimen during the thawing phase: (A) vertical displacement (u_y), (B) cryo-suction (s^*_{cryo}), (C) temperature (θ), and (D) ice saturation (S^i) profiles along the central axis

volumetric expansion due to the phase transition. Since the applied temperature at the top starts to increase after reaching its minimum, s^*_{cryo} tends to decrease after $t = 7.5$ h due to the freezing characteristic function in Equation (31) although the freezing front still propagates towards the bottom. Also, during the freezing phase, soil specimen tends to exhibit a constant temperature distribution at the region below the freezing front due to the latent heat effect, similar to our previous example shown in Section 5.2. More importantly, we observe a sequential development of the ice lenses at $y = 0.092$ m, $y = 0.066$ m, and $y = 0.042$ m, respectively, which implies that separation void ratio (e_{sep}) can be approximated as ~0.75[25]. This result is expected, since those regions possess relatively high initial porosity compared to the other regions (Figure 11A). If the freezing front reaches the porous zone where the critical energy release rate is relatively low, both the cryo-suction and the exerted stress due to the phase transition initiate the horizontal crack.

Once the freezing-induced fracture is developed, segregated bulk ice tends to form inside the opened crack at higher growth rates that lead to an abrupt volume expansion therein (Figure 12). As illustrated in Figure 14, we observe the opposite response during the thawing phase ($11.25\text{ h} \leq t \leq 15\text{ h}$). At $t = 11.25$ h, once the applied temperature at the top again reaches the melting temperature $\theta_m = 273.15$ K, the soil specimen stops freezing and begins to thaw from the top to the bottom. During the thawing process, the melting front tends to move downwards whereas the freezing front remains unchanged since the bottom surface is thermally insulated. As the melted region where $\theta > \theta_m$ evolves, the vertical displacement tends to decrease over time due to both the volume contraction during the phase transition and the water expulsion towards the top surface.

Figure 15 shows the evolution of the vertical displacement of the top surface during the freeze–thaw test (black curve). For comparison, we introduce a control experiment where the phase-field solvers for both ice lens and damage are disabled but otherwise the material parameters are identical (blue curve). Hence, the numerical specimen in the control experiment may exhibit homogeneous freezing and thawing but not ice-lens formation and melting. The frost heave and thawing settlement for both experiments are compared to assess the impact of the ice lenses on the material responses.

In the prime numerical experiment, ice lenses sequentially develop at $y = 0.092$ m, $y = 0.066$ m, and $y = 0.042$ m (see Figure 12), respectively. Each time the ice lens begins to form, the soil expands more rapidly and hence the steeper slope of the black curve, which indicates the rapid expansion of the numerical specimen, at $t = 4.2$ h, $t = 6.2$ h, and $t = 8.8$ h. During the thawing phase, the prescribed temperature of the top surface increase. This temperature increase leads to abrupt settlement within the first 2 h of the thawing phase.As the ice lenses melt and subsequently drain out from the domain, the numerical specimen shrinks (black curve). In contrast, homogeneous freezing and thawing result in considerably less amount of frost heaving and thawing settlement, due to the absence of cracks where ice lenses may form.

The significant difference between the two simulations has important practical implications. It is presumably possible to use an optimization algorithm to identify the material parameters such that the control experiment may match better with the observed frost heave and thawing settlements of soil vulnerable to ice-lens formation. However, the apparent match obtained from such an excessive calibration could be fruitless as it may lead to material parameters that are not physical and therefore make the calibrated model weak at forward predictions. Results of these numerical experiments again suggest that the ice lenses play a key role in frost heaving and the subsequent settlement of soils. This example

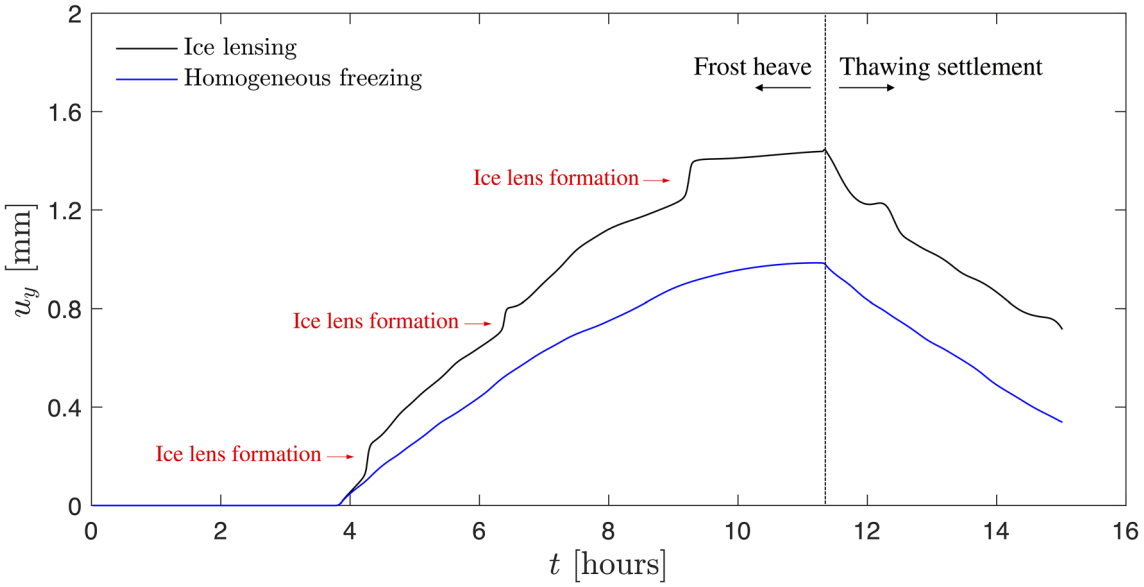

FIGURE 15 Vertical displacement (u_y) evolution of the top surface during the numerical freeze–thaw test. The black curve is obtained from a thermo-hydro-mechanical simulation that enables ice lensing; the blue curve is obtained from the control experiment that takes out the ice lensing capacity

FIGURE 16 Schematic of geometry and boundary conditions for the single edge-notched test

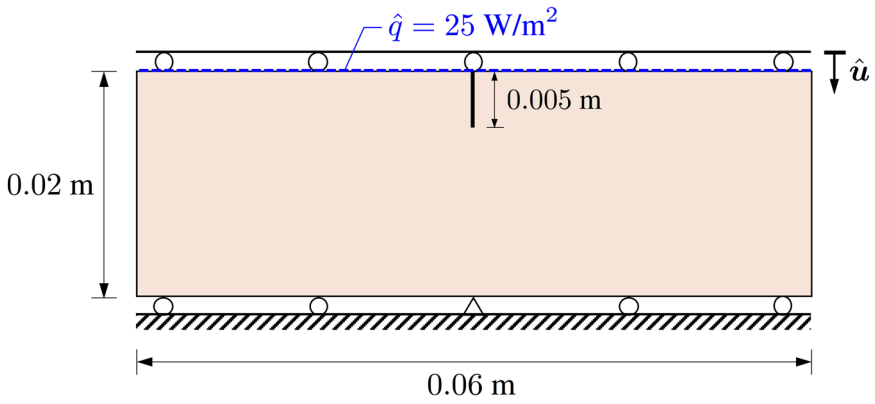

also highlights that our proposed model is capable of simulating the ice-lens growth and thaw in a fluid-saturated porous media.

5.4 | Vertical ice-lens growth in edge-notched specimen

While numerical example presented in Section 5.3 demonstrated horizontal ice-lens formation perpendicular to the freezing direction, in this section, we simulate vertical ice-lens growth, which is parallel to the freezing direction, by leveraging the proposed driving force [Equation (27)] for the Allen–Cahn equation. Specifically, our objective is to demonstrate the formation of an ice lens that follows the crack trajectory that leads to a nonplanar ice growth. Hence, as shown in Figure 16, the problem domain is a 0.06-m-wide and 0.02-m-long rectangular globally undrained porous specimen that contains a 0.005-m-long initial vertical edge notch along the central axis, while considering an ideal case where $\boldsymbol{\sigma}'_{\text{dam}} = \mathbf{0}$ and $\bar{\alpha}_v = 0$ to focus on the ice-lens growth along the crack by decoupling the interactions between the two. By setting the initial temperature as $\theta_0 = 274.15$ K, the numerical experiment is performed by applying a constant heat flux of $\hat{q} = 25$ W/m^2 that induces conductive vertical cooling from the top surface, with prescribed vertical displacement $\hat{\boldsymbol{u}}$ at a rate of -10^{-6} mm/s to promote crack growth from the notch tip. Here, we assume that the material is homogeneous while the material parameters are chosen as follows: $\phi_0 = 0.2$, $\rho_s = 2500$ kg/m^3, $\rho_w = 1000$ kg/m^3, $\rho_i = 920$ kg/m^3, $E = 2.5$ GPa, $\nu = 0.3$, $k_{\text{mat}} = 10^{-15}$ m^2, $\mu_w = 10^{-3}$ Pa·s, $c_s = 0.9 \times 10^3$ J/kg/K, $c_w = 4.2 \times 10^3$ J/kg/K, $c_i = 1.9 \times 10^3$ J/kg/K, $\kappa_s = 7.55$ W/m/K,

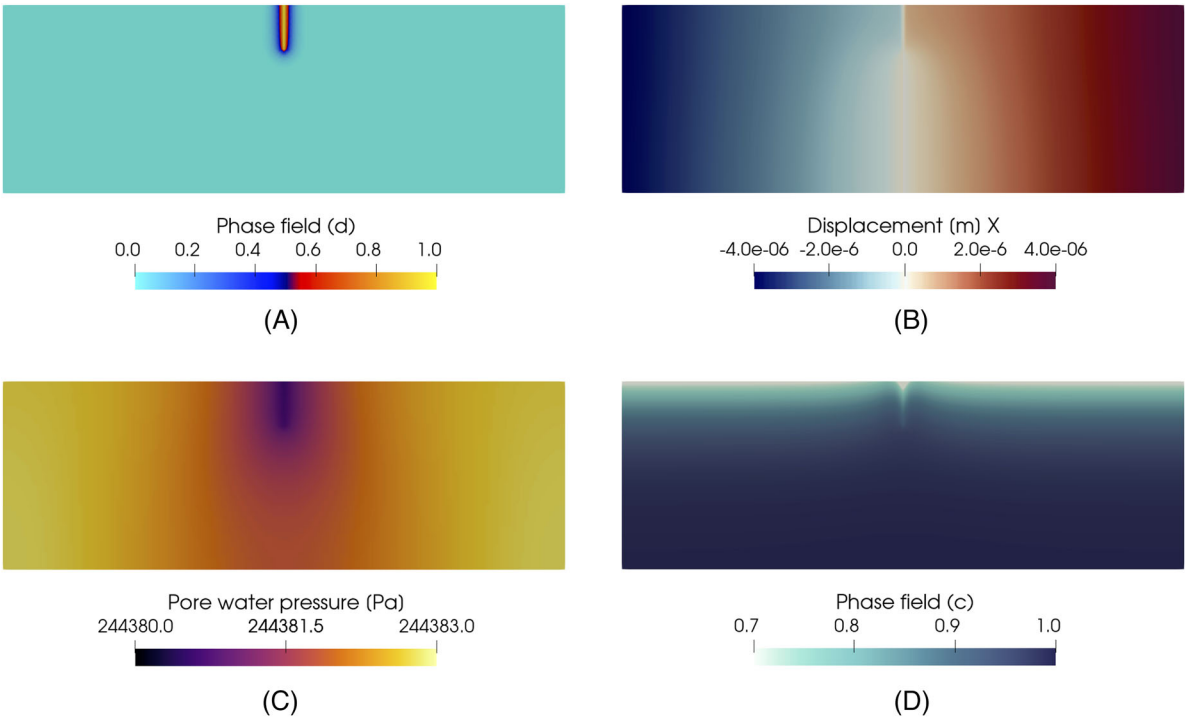

FIGURE 17 Transient response of porous specimen at $t = 45$ min. (A) Fracture phase field d; (B) x-displacement u_x; (C) pore water pressure p_w; and (D) Allen–Cahn phase field c

$\kappa_w = 0.5$ W/m/K, $\kappa_i = 2.25$ W/m/K, $\mathcal{G}_d = 2.25$ N/m, $l_d = 1.0 \times 10^{-3}$ m, $K_c^* = 5.0 \times 10^9$ Pa, and $g_c^* = 1.25$. In addition, we set $\nu_c = 0.0001$, $\gamma_c = 0.05\,\text{J/m}^2$, $\delta_c = 0.0001$ m, and $\epsilon_c = 0.5\,(\text{J/m})^{1/2}$ for the Allen–Cahn phase-field model while adopting the structured mesh with element size of $h_e = 0.25$ mm and the time step size of $\Delta t = 1$ min.

Based on this setting, as shown in Figure 17, prescribed compression results in tensile stresses perpendicular to the loading direction that stimulates crack growth, while permeability enhancement [Equation (46)] and relative permeability [Equation (39)] yield relatively low pore water pressure inside the notch similar to the results shown in Hyoung Suk et al.[109] The phase transition process of pore water begins once the temperature at the top surface reaches the freezing temperature θ_m in both the damaged and undamaged regions, however, since the proposed driving force for the Allen-Cahn equation in Equation (27) leads to an intense growth of ice inside the fracture (i.e., ice lens) such that the phase-field c tends to evolve faster inside the damaged region (Figure 17A,D).

As evidenced in Figure 17D, ice phase tends to continuously grow along the pre-existing notch until crack initiates from the tip. Then, as illustrated in Figure 18, once crack starts to propagate due to the combined effect of ice–water-phase transition and the applied load, ice lens tends to follow the crack trajectory. We can also see from Figure 18 that crack opening leads to complete fragmentation of the solid matrix due to the relation shown in Equation (48), which results in more realistic ice-lens simulations since it possesses zero solidity, that is, $1 - \phi$. More importantly, the results indicate that our proposed framework is not only restricted to simulating planar ice lenses but also capable of modeling nonplanar ice lenses that are not necessarily perpendicular to the freezing direction, which may have a more profound impact on microporomechanical problems that involve water adsorption processes, which can affect microscopic fluid motion inside the heterogeneous matrix and hence the freezing patterns.

6 | CONCLUSIONS

We introduce a multiphase-field microporomechanics theory and the corresponding finite element solver to capture the freeze–thaw action in a frozen/freezing/thawing porous medium that may form ice lenses. By introducing two-phase field variables that indicate the phase of the ice/water and damaged/undamaged material state, the proposed thermo-hydro-mechanical model is capable of simulating the freezing-induced fracture caused by the growth of the ice lens as segregated ice. We also extend the Bishop's effective stress principle for frozen soil to incorporate the effects of damage and ice growth

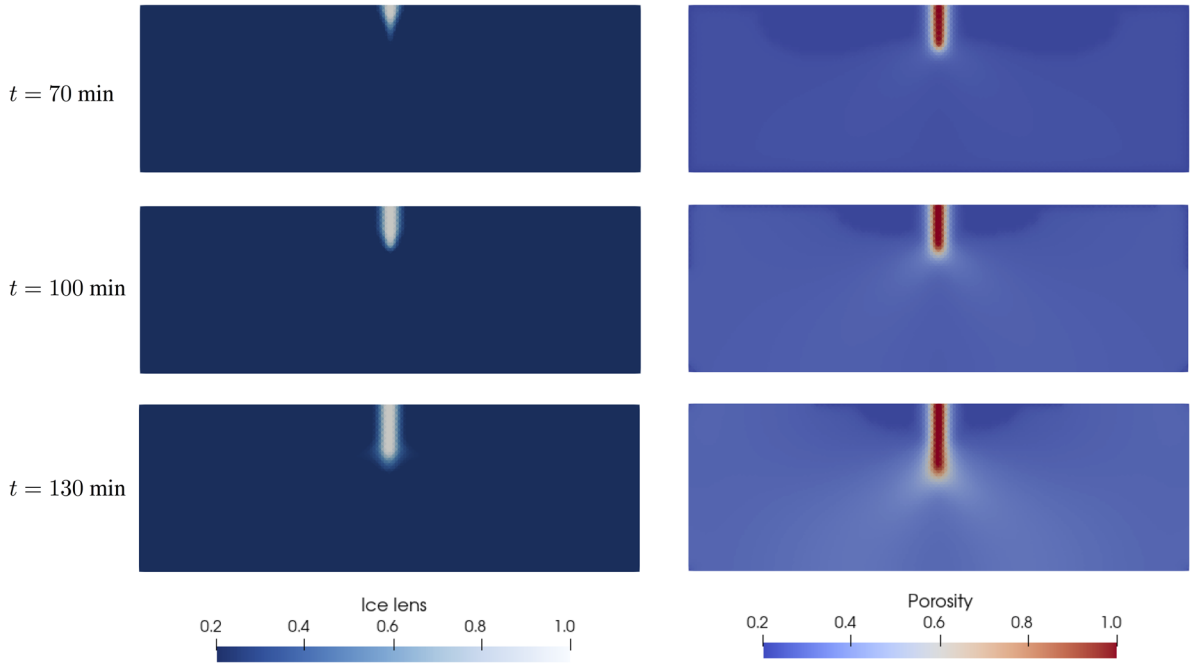

FIGURE 18 Evolution of ice lens (χ^i) and porosity (ϕ) during vertical freezing of edge-notched specimen

and distinguish them from those of the freezing retention responses. This treatment enables us to take into account the shear strength of the ice lenses and analyzes how the homogeneous freezing process and the ice-lens growth affect the thermo-hydro-mechanical coupling effects in the transient regime. The model is validated against published freezing experiments. To investigate how the formation and thawing of ice lens affect the frost heave and thaw settlement, we conduct numerical experiments that simulate the climate-induced frozen heave and thaw settlement in one thermal cycle and compare the simulation results with those obtained from a thermo-hydro-mechanical model that does not explicitly capture the ice lens. The simulation results suggest that explicitly capturing the growth and thaw of ice lens may provide more precise predictions and analyses on the multi-physical coupling effects of frozen soil at different time scales. Accurate and precise predictions on the frozen heave and thaw settlement are crucial for many modern engineering applications, from estimating the durability of pavement systems to the exploration of ice-rich portions of Mars. This work provides a foundation for a more precise depiction of frozen soil by incorporating freezing retention, heat transfer, fluid diffusion, fracture mechanics, and ice-lens growth in a single model. More accurate predictions nevertheless may require sufficient data to solve the inverse problems and quantify uncertainties as well as optimization techniques to identify material parameters from different experiments. Such endeavors are important and will be considered in the future studies.

ACKNOWLEDGMENTS

This work is primarily supported by the Earth Materials and Processes program from the US Army Research Office under grant contract W911NF-18-2-0306, with additional time of the PI supported by the NSF CAREER grant from Mechanics of Materials and Structures program at National Science Foundation under grant contract CMMI-1846875. These supports are gratefully acknowledged. The views and conclusions contained in this document are those of the authors, and should not be interpreted as representing the official policies, either expressed or implied, of the sponsors, including the Army Research Laboratory or the U.S. Government. The U.S. Government is authorized to reproduce and distribute reprints for Government purposes notwithstanding any copyright notation herein.

DATA AVAILABILITY STATEMENT

The source codes and data generated during and/or analyzed during the current study are available from the corresponding author upon reasonable request.

ORCID

Hyoung Suk Suh https://orcid.org/0000-0002-5032-5255
WaiChing Sun https://orcid.org/0000-0002-3078-5086

REFERENCES

1. Palmer AC, Williams PJ. Frost heave and pipeline upheaval buckling. *Can Geotech J*. 2003;40:1033–1038.
2. Zhang S, Sheng D, Zhao G, Niu F, He Z. Analysis of frost heave mechanisms in a high-speed railway embankment. *Can Geotech J*. 2016;53:520–529.
3. Li A, Niu F, Zheng H, Akagawa S, Lin Z, Luo J. Experimental measurement and numerical simulation of frost heave in saturated coarse-grained soil. *Cold Reg Sci Technol*. 2017;137:68–74.
4. Lake CB, Yousif MAM, Jamshidi RJ. Examining freeze/thaw effects on performance and morphology of a lightly cemented soil. *Cold Reg Sci Technol*. 2017;134:33–44.
5. Ji Y, Zhou G, Zhou Y, Vandeginste V. Frost heave in freezing soils: a quasi-static model for ice lens growth. *Cold Reg Sci Technol*. 2019;158:10–17.
6. DiMillio AF. *A Quarter Century of Geotechnical Research*. Technical report. Turner–Fairbank Highway Research Center; 1999.
7. Nelson FE, Anisimov OA, Shiklomanov NI. Subsidence risk from thawing permafrost. *Nature*. 2001;410:889–890.
8. Nelson FE, Anisimov OA, Shiklomanov NI. Climate change and hazard zonation in the circum-Arctic permafrost regions. *Nat Hazard*. 2002;26:203–225.
9. Streletskiy DA, Shiklomanov NI, Nelson FE. Permafrost, infrastructure, and climate change: a GIS-based landscape approach to geotechnical modeling. *Arct Antarct Alp Res*. 2012;44:368–380.
10. Leibman M, Khomutov A, Kizyakov A. Cryogenic landslides in the West-Siberian plain of Russia: classification, mechanisms, and landforms. In: *Landslides in Cold Regions in the Context of Climate Change*. Springer; 2014:143–162.
11. Mithan H, Hales T, Cleall P. Topographic and ground-ice controls on shallow landsliding in thawing arctic permafrost. *Geophys Res Lett*. 2021;48:e2020GL092264.
12. Taber S. Frost heaving. *J Geol*. 1929;37:428–461.
13. Taber S. The mechanics of frost heaving. *J Geol*. 1930;38:303–317.
14. Peppin SSL, Style RW. The physics of frost heave and ice-lens growth. *Vadose Zone J*. 2013;12(1):1–12.
15. Wilen L, Dash J. Frost heave dynamics at a single crystal interface. *Phys Rev Lett*. 1995;74:5076.
16. Dash J, Fu H, Wettlaufer J. The premelting of ice and its environmental consequences. *Rep Prog Phys*. 1995;58:115.
17. Dash J, Rempel A, Wettlaufer J. The physics of premelted ice and its geophysical consequences. *Rev Mod Phys*. 2006;78:695–741.
18. Harlan R. Analysis of coupled heat-fluid transport in partially frozen soil. *Water Resour Res*. 1973;9:1314–1323.
19. Miller R. Freezing and heaving of saturated and unsaturated soils. *Highway Res Record*. 1972;393:1–11.
20. Miller R. Lens initiation in secondary heaving. In: Proceedings of the International Symposium on Frost Action in Soils, Luleå, Sweden. Luleå Alltryck AB; 1977;2:68–74.
21. O'Neill K, Miller RD. Exploration of a rigid ice model of frost heave. *Water Resour Res*. 1985;21:281–296.
22. Fowler A. Secondary frost heave in freezing soils. *SIAM J Appl Math*. 1989;49:991–1008.
23. Fowler AC, Krantz WB. A generalized secondary frost heave model. *SIAM J Appl Math*. 1994;54:1650–1675.
24. Gilpin R. A model for the prediction of ice lensing and frost heave in soils. *Water Resour Res*. 1980;16:918–930.
25. Zhou J, Li D. Numerical analysis of coupled water, heat and stress in saturated freezing soil. *Cold Reg Sci Technol*. 2012;72:43–49.
26. Konrad JM, Morgenstern NR. A mechanistic theory of ice lens formation in fine-grained soils. *Can Geotech J*. 1980;17:473–486.
27. Nixon JF. Field frost heave predictions using the segregation potential concept. *Can Geotech J*. 1982;19:526–529.
28. Konrad JM, Shen M. 2-D frost action modeling using the segregation potential of soils. *Cold Reg Sci Technol*. 1996;24:263–278.
29. Tiedje E, Guo P. Frost heave modeling using a modified segregation potential approach. In: Proceedings of the Cold Regions Engineering 2012: Sustainable Infrastructure Development in a Changing Cold Environment. 2012:686–696.
30. Rempel AW, Wettlaufer J, Worster MG. Premelting dynamics in a continuum model of frost heave. *J Fluid Mech*. 2004;498:227–244.
31. Rempel A. Formation of ice lenses and frost heave. *J Geophys Res: Earth Surf*. 2007;112(F2):F02S21.
32. Style RW, Peppin SS, Cocks AC, Wettlaufer JS. Ice-lens formation and geometrical supercooling in soils and other colloidal materials. *Phys Rev E*. 2011;84:041402.
33. Nishimura S, Gens A, Olivella S, Jardine R. THM-coupled finite element analysis of frozen soil: formulation and application. *Géotechnique*. 2009;59:159–171.
34. Zhou M, Meschke G. A three-phase thermo-hydro-mechanical finite element model for freezing soils. *Int J Numer Anal Methods Geomech*. 2013;37:3173–3193.
35. Na S, Sun W. Computational thermo-hydro-mechanics for multiphase freezing and thawing porous media in the finite deformation range. *Comput Meth Appl Mech Eng*. 2017;318:667–700.
36. Michalowski RL, Zhu M. Frost heave modelling using porosity rate function. *Int J Numer Anal Methods Geomech*. 2006;30:703–722.
37. Ghoreishian Amiri S, Grimstad G, Kadivar M, Nordal S. Constitutive model for rate-independent behavior of saturated frozen soils. *Can Geotech J*. 2016;53:1646–1657.
38. Wettlaufer J, Worster MG. Premelting dynamics. *Annu. Rev. Fluid Mech*. 2006;38:427–452.
39. Allen SM, Cahn JW. A microscopic theory for antiphase boundary motion and its application to antiphase domain coarsening. *Acta Metall*. 1979;27:1085–1095.
40. Boettinger WJ, Warren JA, Beckermann C, Karma A. Phase-field simulation of solidification. *Annu Rev Mater Res*. 2002;32:163–194.
41. Bourdin B, Francfort GA, Marigo JJ. The variational approach to fracture. *J Elast*. 2008;91(1-3):5–148.

42. Miehe C, Hofacker M, Welschinger F. A phase field model for rate-independent crack propagation: robust algorithmic implementation based on operator splits. *Comput Meth Appl Mech Eng*. 2010;199(45-48):2765–2778.
43. Borden MJ, Verhoosel CV, Scott MA, Hughes TJ, Landis CM. A phase-field description of dynamic brittle fracture. *Comput Meth Appl Mech Eng*. 2012;217:77–95.
44. Warren JA, Boettinger WJ. Prediction of dendritic growth and microsegregation patterns in a binary alloy using the phase-field method. *Acta Metall Mater*. 1995;43:689–703.
45. Sweidan AH, Heider Y, Markert B. A unified water/ice kinematics approach for phase-field thermo-hydro-mechanical modeling of frost action in porous media. *Comput Meth Appl Mech Eng*. 2020;372:113358.
46. Chaboche JL. Continuum damage mechanics: part I—general concepts. *ASME. J. Appl. Mech.* 1988;55(1):59–64. https://doi.org/10.1115/1.3173661
47. Bowen RM. Incompressible porous media models by use of the theory of mixtures. *Int J Eng Sci*. 1980;18:1129–1148.
48. Zienkiewicz OC, Chan A, Pastor M, Schrefler B, Shiomi T. *Computational Geomechanics*. Citeseer; 1999:613.
49. Ehlers W. Foundations of multiphasic and porous materials. In: *Porous Media*. Springer; 2002:3–86.
50. Coussy O. *Poromechanics*. John Wiley & Sons; 2004.
51. O'Neill K. *Numerical Solutions for a Rigid-ice Model of Secondary Frost Heave*. 82. US Army Corps of Engineers: Cold Regions Research & Engineering Laboratory; 1982.
52. Suh HS, Sun W, O'Connor DT. A phase field model for cohesive fracture in micropolar continua. *Comput Methods Appl Mech Eng*. 2020;369:113181.
53. Miehe C, Welschinger F, Hofacker M. Thermodynamically consistent phase-field models of fracture: variational principles and multi-field FE implementations. *Int J Numer Methods Eng*. 2010;83:1273–1311.
54. Choo J, Sun W. Cracking and damage from crystallization in pores: coupled chemo-hydro-mechanics and phase-field modeling. *Comput Methods Appl Mech Eng*. 2018;335:347–379.
55. Heider Y. A review on phase-field modeling of hydraulic fracturing. *Eng Fract Mech*. 2021;253:107881.
56. Bryant EC, Sun W. A mixed-mode phase field fracture model in anisotropic rocks with consistent kinematics. *Comput Methods Appl Mech Eng*. 2018;342:561–584.
57. Suh HS, Sun W. Asynchronous phase field fracture model for porous media with thermally non-equilibrated constituents. *Comput Methods Appl Mech Eng*. 2021;387:114182.
58. Borja RI, Yin Q, Zhao Y. Cam-Clay plasticity. Part IX: on the anisotropy, heterogeneity, and viscoplasticity of shale. *Comput Methods Appl Mech Eng*. 2020;360:112695.
59. Bluhm J, Ricken T. Modeling of freezing and thawing processes in liquid filled thermo-elastic porous solids. In: Setzer M, ed. *Transport in Concrete: Nano-to Macrostructure*. Aedificatio Publishers; 2007:41–57.
60. Ricken T, Bluhm J. Modeling fluid saturated porous media under frost attack. *GAMM-Mitteilungen*. 2010;33:40–56.
61. Van Genuchten MT. A closed-form equation for predicting the hydraulic conductivity of unsaturated soils. *Soil Sci Soc Am J*. 1980;44:892–898.
62. Gelet R, Loret B, Khalili N. A thermo-hydro-mechanical coupled model in local thermal non-equilibrium for fractured HDR reservoir with double porosity. *J Geophys Res Solid Earth*. 2012;117(B7):1–23.
63. Liu Z, Muldrew K, Wan RG, Elliott JA. Measurement of freezing point depression of water in glass capillaries and the associated ice front shape. *Phys Rev E*. 2003;67:061602.
64. Loginova I, Amberg G, Ågren J. Phase-field simulations of non-isothermal binary alloy solidification. *Acta Materialia*. 2001;49:573–581.
65. Alexiades V, Solomon AD. *Mathematical Modeling of Melting and Freezing Processes*. Routledge; 2018.
66. Eshelby JD. The determination of the elastic field of an ellipsoidal inclusion, and related problems. *Proc R Soc London, A*. 1957;241:376–396.
67. Hiroshi H, Minoru T. Equivalent inclusion method for steady state heat conduction in composites. *Int J Eng Sci*. 1986;24:1159–1172.
68. Sun W. A stabilized finite element formulation for monolithic thermo-hydro-mechanical simulations at finite strain. *Int J Numer Methods Eng*. 2015;103:798–839.
69. Lee C, Suh HS, Yoon B, Yun TS. Particle shape effect on thermal conductivity and shear wave velocity in sands. *Acta Geotech*. 2017;12:615–625.
70. Suh HS, Yun TS. Modification of capillary pressure by considering pore throat geometry with the effects of particle shape and packing features on water retention curves for uniformly graded sands. *Comput Geotech*. 2018;95:129–136.
71. Takaki T. Phase-field modeling and simulations of dendrite growth. *ISIJ Int*. 2014;54:437–444.
72. Aihara S, Takaki T, Takada N. Multi-phase-field modeling using a conservative Allen–Cahn equation for multiphase flow. *Comput Fluid*. 2019;178:141–151.
73. Henry KS. *A Review of the Thermodynamics of Frost Heave*. 2000.
74. Wheeler AA, Boettinger WJ, McFadden GB. Phase-field model for isothermal phase transitions in binary alloys. *Phys Rev A*. 1992;45:7424–7439.
75. Caginalp G, Socolovsky E. Efficient computation of a sharp interface by spreading via phase field methods. *Appl Math Lett*. 1989;2:117–120.
76. Caginalp G, Socolovsky E. Computation of sharp phase boundaries by spreading: the planar and spherically symmetric cases. *J Comput Phys*. 1991;95:85–100.
77. Penner E. Aspects of ice lens growth in soils. *Cold Reg Sci Technol*. 1986;13:91–100.

78. Espinosa RM, Franke L, Deckelmann G. Phase changes of salts in porous materials: crystallization, hydration and deliquescence. *Constr Build Mater*. 2008;22:1758–1773.
79. Koniorczyk M, Gawin D. Modelling of salt crystallization in building materials with microstructure—poromechanical approach. *Constr Build Mater*. 2012;36:860–873.
80. Derluyn H, Moonen P, Carmeliet J. Deformation and damage due to drying-induced salt crystallization in porous limestone. *J Mech Phys Solids*. 2014;63:242–255.
81. Guodong C. The mechanism of repeated-segregation for the formation of thick layered ground ice. *Cold Reg Sci Technol*. 1983;8:57–66.
82. Harris C, Arenson LU, Christiansen HH, et al. Permafrost and climate in Europe: monitoring and modelling thermal, geomorphological and geotechnical responses. *Earth Sci Rev*. 2009;92(3-4):117–171.
83. Evans B, Fredrich JT, Wong TF. *The Brittle–Ductile Transition in Rocks: Recent Experimental and Theoretical Progress, Geophysical Monograph Series*. Vol. 56. 1990:1–20.
84. Lee MY, Fossum A, Costin LS, Bronowski D. *Frozen Soil Material Testing and Constitutive Modeling*. Sandia report 524. SAND; 2002:8–65.
85. Anderson DM, Tice AR. Predicting unfrozen water contents in frozen soils from surface area measurements. *Highway Res Record*. 1972;393:12–18.
86. Koopmans RWR, Miller R. Soil freezing and soil water characteristic curves. *Soil Sci Soc Am J*. 1966;30:680–685.
87. Black PB, Tice AR. Comparison of soil freezing curve and soil water curve data for Windsor sandy loam. *Water Resour Res*. 1989;25:2205–2210.
88. Ma T, Wei C, Xia X, Zhou J, Chen P. Soil freezing and soil water retention characteristics: connection and solute effects. *J Perform Constr Facil*. 2017;31:D4015001.
89. Bai R, Lai Y, Zhang M, Yu F. Theory and application of a novel soil freezing characteristic curve. *Appl Therm Eng*. 2018;129:1106–1114.
90. Luckner L, Van Genuchten MT, Nielsen D. A consistent set of parametric models for the two-phase flow of immiscible fluids in the subsurface. *Water Resour Res*. 1989;25:2187–2193.
91. Seyfried M, Murdock M. Use of air permeability to estimate infiltrability of frozen soil. *J Hydrol*. 1997;202(1-4):95–107.
92. Demand D, Selker JS, Weiler M. Influences of macropores on infiltration into seasonally frozen soil. *Vadose Zone J*. 2019;18:1–14.
93. Eigenbrod K. Self-healing in fractured fine-grained soils. *Can Geotech J*. 2003;40:435–449.
94. Foriero A, Ladanyi B. FEM assessment of large-strain thaw consolidation. *J Geotech Eng*. 1995;121:126–138.
95. Zhang Y, Michalowski RL. Thermal-hydro-mechanical analysis of frost heave and thaw settlement. *J Geotech Geoenviron Eng*. 2015;141:04015027.
96. Dittmann M, Krüger M, Schmidt F, Schuß S, Hesch C. Variational modeling of thermomechanical fracture and anisotropic frictional mortar contact problems with adhesion. *Comput Mech*. 2019;63:571–591.
97. Dittmann M, Aldakheel F, Schulte J, et al. Phase-field modeling of porous-ductile fracture in non-linear thermo-elasto-plastic solids. *Comput Meth Appl Mech Eng*. 2020;361:112730.
98. Miehe C, Mauthe S, Teichtmeister S. Minimization principles for the coupled problem of Darcy–Biot-type fluid transport in porous media linked to phase field modeling of fracture. *J Mech Phys Solids*. 2015;82:186–217.
99. Amor H, Marigo JJ, Maurini C. Regularized formulation of the variational brittle fracture with unilateral contact: numerical experiments. *J Mech Phys Solids*. 2009;57:1209–1229.
100. Miehe C, Schaenzel LM, Ulmer H. Phase field modeling of fracture in multi-physics problems. Part I. Balance of crack surface and failure criteria for brittle crack propagation in thermo-elastic solids. *Comput Meth Appl Mech Eng*. 2015;294:449–485.
101. Suh HS, Sun W. An open-source FEniCS implementation of a phase field fracture model for micropolar continua. *Int J Multiscale Comput Eng*. 2019;17(6):639–663.
102. Bryant EC, Sun W. Phase field modeling of frictional slip with slip weakening/strengthening under non-isothermal conditions. *Comput Methods Appl Mech Eng*. 2021;375:113557.
103. Viklander P. Permeability and volume changes in till due to cyclic freeze/thaw. *Can Geotech J*. 1998;35:471–477.
104. Rayhani M, Yanful E, Fakher A. Physical modeling of desiccation cracking in plastic soils. *Eng Geol*. 2008;97(1-2):25–31.
105. Ma R, Sun W. Computational thermomechanics for crystalline rock. Part II: chemo-damage-plasticity and healing in strongly anisotropic polycrystals. *Comput Methods Appl Mech Eng*. 2020;369:113184.
106. Miehe C, Mauthe S. Phase field modeling of fracture in multi-physics problems. Part III. Crack driving forces in hydro-poro-elasticity and hydraulic fracturing of fluid-saturated porous media. *Comput Methods Appl Mech Eng*. 2016;304:619–655.
107. Mauthe S, Miehe C. Hydraulic fracture in poro-hydro-elastic media. *Mech Res Commun*. 2017;80:69–83.
108. Wang K, Sun W. A unified variational eigen-erosion framework for interacting brittle fractures and compaction bands in fluid-infiltrating porous media. *Comput Methods Appl Mech Eng*. 2017;318:1–32.
109. Suh HS, Sun W. An immersed phase field fracture model for microporomechanics with Darcy–Stokes flow. *Phys Fluids*. 2021;33:016603.
110. Wilson ZA, Landis CM. Phase-field modeling of hydraulic fracture. *J Mech Phys Solids*. 2016;96:264–290.
111. Heider Y, Sun W. A phase field framework for capillary-induced fracture in unsaturated porous media: drying-induced vs. hydraulic cracking. *Comput Methods Appl Mech Eng*. 2020;359:112647.
112. Bouddour A, Auriault J, Mhamdi-Alaoui M. Erosion and deposition of solid particles in porous media: homogenization analysis of a formation damage. *Transp Porous Media*. 1996;25:121–146.
113. Bonelli S, Brivois O. The scaling law in the hole erosion test with a constant pressure drop. *Int J Numer Anal Methods Geomech*. 2008;32:1573–1595.

114. Sterpi D. Effects of the erosion and transport of fine particles due to seepage flow. *Int J Geomech*. 2003;3:111–122.
115. Pope S. A more general effective-viscosity hypothesis. *J Fluid Mech*. 1975;72:331–340.
116. Simo J, Miehe C. Associative coupled thermoplasticity at finite strains: formulation, numerical analysis and implementation. *Comput Methods Appl Mech Eng*. 1992;98:41–104.
117. Nguyen T, Selvadurai A. Coupled thermal-mechanical-hydrological behaviour of sparsely fractured rock: implications for nuclear fuel waste disposal. *Int J Rock Mech Min Sci Geomech Abstr*. 1995;32:465–479.
118. Logg A, Wells GN. DOLFIN: Automated finite element computing. *ACM Trans Math Softw*. 2010;37:1–28.
119. Logg A, Mardal KA, Wells G. *Automated Solution of Differential Equations by the Finite Element Method: The FEniCS Book*. Vol. 84. Springer Science & Business Media; 2012.
120. Alnæs M, Blechta J, Hake J, et al. The FEniCS project version 1.5. *Arch Numer Softw*. 2015;3(100):9–23.
121. Abhyankar S, Brown J, Constantinescu EM, Ghosh D, Smith BF, Zhang H. PETSc/TS: a modern scalable ODE/DAE solver library. *arXiv preprint arXiv:1806.01437*. 2018.
122. Sweidan A, Niggemann K, Heider Y, Ziegler M, Markert B. Experimental study and numerical modeling of the thermo-hydro-mechanical processes in soil freezing with different frost penetration directions. *Acta Geotech*. 2021;17:231–255.
123. Feng S, Zhang Y, Shi M, Wen T, Lu TJ. Unidirectional freezing of phase change materials saturated in open-cell metal foams. *Appl Therm Eng*. 2015;88:315–321.
124. Lackner R, Amon A, Lagger H. Artificial ground freezing of fully saturated soil: thermal problem. *J Eng Mech*. 2005;131:211–220.
125. Terzaghi K, Peck RB, Mesri G. *Soil Mechanics*. John Wiley & Sons; 1996.
126. Amato G, Andò E, Lyu C, Viggiani G, Eiksund GR. A glimpse into rapid freezing processes in clay with x-ray tomography. *Acta Geotech*. 2021;17:327–338.
127. Uyanık O. Estimation of the porosity of clay soils using seismic P- and S-wave velocities. *J Appl Geophys*. 2019;170:103832.
128. Dunn DE, LaFountain LJ, Jackson RE. Porosity dependence and mechanism of brittle fracture in sandstones. *J Geophys Res*. 1973;78:2403–2417.
129. Karma A, Rappel WJ. Phase-field method for computationally efficient modeling of solidification with arbitrary interface kinetics. *Phys Rev E*. 1996;53:R3017–R3020.

How to cite this article: Suh H.S., Sun W. Multiphase-field microporomechanics model for simulating ice-lens growth in frozen soil. *Int J Numer Anal Methods*. 2022;46:2307–2336. https://doi.org/10.1002/nag.3408

APPENDIX A: RELATIONSHIP AMONG THE ALLEN-CAHN MODEL PARAMETERS AND PHYSICAL PROPERTIES

In this section, we consider an idealized one-dimensional transition zone between water ($c = 1$) and ice ($c = 0$) phase constituents to obtain the relationship among the parameters (Equation (26)) for the Allen–Cahn phase field equation. Here, we assume planar ice–water transition zone, where the phase field c varies along the x direction. Since $\nabla^2 c = \partial^2 c/\partial x^2$ in one-dimensional setting, an equilibrium solution ($\dot{c} = 0$) at the freezing temperature $\theta = \theta_m$ can be obtained as follows:

$$c(x) = \frac{1}{2}\left[1 + \tanh\left(\frac{x}{2\delta_c}\right)\right], \tag{A1}$$

where δ_c is a measure of interface thickness which can be expressed as[40,44]:

$$\delta_c = \frac{\epsilon_c}{\sqrt{2W_c}}. \tag{A2}$$

As pointed out in Boettinger et al.,[40] the interface thickness δ_c balances two opposing effects. The transition zone tends to become narrow depending on the energy hump parameter W_c, and at the same time tends to be diffusive in order to reduce the energy associated with ∇c, based on the coefficient ϵ_c. From Equations (A1) and (A2), Figure A1 illustrates the variations of the phase field c and the integrand of Equation (20) normalized by W_c along the distance x across a flat ice–water interface at the freezing temperature. Since the area under the curve shown in Figure A1B is the ice–water interface energy (i.e., interfacial tension γ_{iw}),[39] we can obtain the first two expressions in Equation (26) by taking the limit $\delta_c \to 0$ while keeping γ_{iw} fixed.

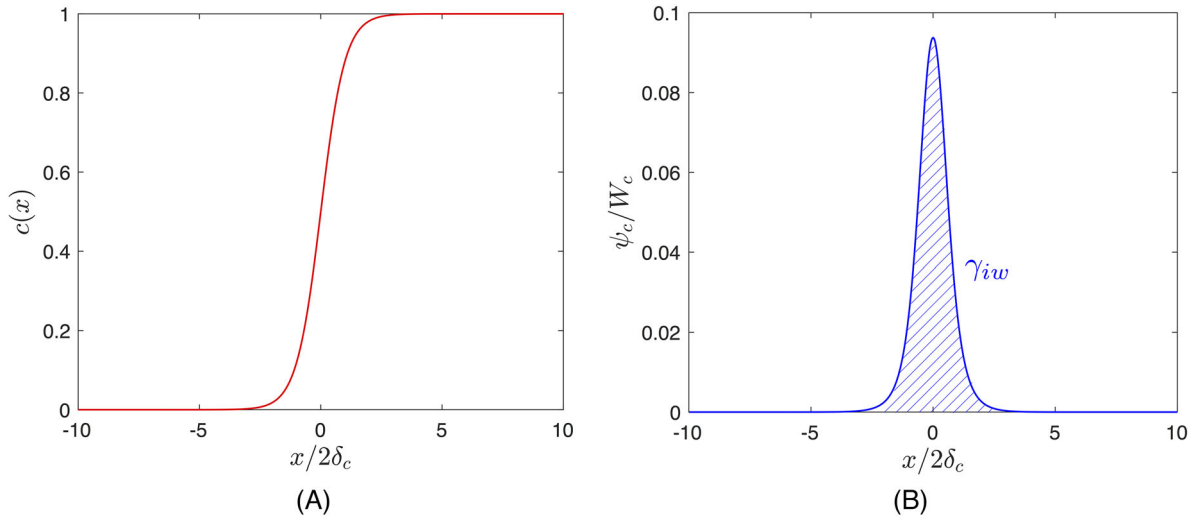

FIGURE A1 Variations of (A) phase-field variable c and (B) the normalized energy density with distance x, across a flat ice–water interface

On the other hand, to investigate a moving interface in one-dimensional space, we consider the case where c moves at a constant velocity v_0 while neglecting the diffusion process. In this case, we can assume that

$$\dot{c} = -v_0 \frac{\partial c}{\partial x}, \tag{A3}$$

and substituting Equation (A3) into Equation (21) yields the following expression:

$$\frac{v_0}{M_c}\left(\frac{\partial c}{\partial x}\right) = \frac{\partial f_c}{\partial c}. \tag{A4}$$

Note that Equation (A4) has no solution if $\theta = \theta_m$, however, a solution does exist for a small δ_c if the temperature is given by Refs.[40,129]

$$\theta = \theta_m - \frac{v_0}{\nu_c}. \tag{A5}$$

In this case, the kinetic coefficient ν_c can be estimated as Wheeler et al.[74]:

$$\nu_c = \frac{6M_c\rho_i L_\theta \epsilon_c}{\theta_m \sqrt{2W_c}}. \tag{A6}$$

By rearranging Equation (A6), the expression for the parameter M_c in Equation (26) can be obtained.